Processes of Breaking of Large-Amplitude Unsteady Lee Waves Leading to Turbulence

S. Abe and T. Nakamura

S. Abe, Graduate School of Environmental Science, Hokkaido University, N10W5, Kita-ku, Sapporo 060-0810, Japan (abe-s@lowtem.hokudai.ac.jp)

T. Nakamura, Pan-Okhotsk Research Center, Institute of Low Temperature Science, Hokkaido University, Kita-19, Nishi-8, Kita-ku, Sapporo 060-0819, Japan (nakamura@lowtem.hokudai.ac.jp)

Abstract

The transition to turbulence after excitation of large-amplitude (~200 m) unsteady lee waves in Amchitka Pass, Alaska, is investigated using a nonhydrostatic vertically two-dimensional model with realistic topography. The model resolves motions two orders smaller than a large-amplitude unsteady lee wave, which is excited in the lee of the ridge, and shows that transition processes near the ridge top and downstream of the first trough of the unsteady lee wave are different. Near the ridge top, three stages of transition are identified. In the first stage, convection begins on the upstream sides (forward wave breaking) and downstream sides (backward wave breaking) of the crests of the unsteady lee wave. In the next stage, Kelvin-Helmholtz (KH) waves develop in regions of enhanced shear between statically unstable regions and downslope flow on the bottom. In the last stage, Tollmien-Schlichting (TS) waves develop on the bottom, under the KH waves, and form vortices, which finally break down. To the best of the authors' knowledge, this is the first paper to report the occurrence of backward wave breaking and the possibility of TS wave excitation in the ocean. Downstream of the first trough of the unsteady lee wave, flow is separated from the bottom by an adverse pressure gradient attributed to the unsteady lee wave. The separated flow forms vortices, which are shed quasi-periodically. Diapycnal mixing is enhanced by the development of KH and TS waves and flow separation, as well as by convection due to overturning isopycnals induced by the unsteady lee wave.

1. Introduction

Breaking internal waves are a major energy source for diapycnal mixing in the ocean, which is an important process that determines the patterns and strengths of global and basin-scale thermohaline circulations [e.g., *Munk and Wunsch*, 1998]. In particular, breaking of large-amplitude lee waves (amplitude $\gtrsim$100 m) cause vigorous diapycnal mixing, which is hundreds to tens of thousands times as intense as that in the open ocean. Lee waves are a kind of internal waves generated by a flow over topographic features and often grow enough to break at the generation sites, because their horizontal phase speed is equal to the flow but in the opposite direction. In fact, observations and model experiments have shown intense mixing due to breaking of large-amplitude lee waves generated by diurnal tides in the Aleutian Passes [*Nakamura et al.,* 2010] and the Kuril Straits [e.g., *Nakamura et al.,* 2000], and by semidiurnal tides in the Knight Inlet sill, British Columbia [e.g., *Farmer and Freeland*, 1983], the Hawaiian ridge [*Klymak et al.*, 2008], and the Oregon continental slope [*Nash et al*., 2007]. Large-amplitude lee waves are also expected to be excited in other regions having ridges, shelf breaks, or sea mounts by diurnal [*Nakamura et al*., 2010] or semidiurnal tides [*Legg and Klymak*, 2008].

Because the breaking, large-amplitude lee waves and the turbulence that causes mixing differ greatly in terms of their spatial scales, some transition processes are expected to occur between the lee waves and the turbulence. Such processes were indeed observed in simulations of atmospheric lee waves in studies [e.g., *Scinocca and Peltier,* 1993] of the evolution of an unstable solution of a steady lee wave initialized by *Long's* [1953] analytical solution. The results showed that, first, convection occurs in a density inversion region caused by a large-amplitude lee wave and forms a pool of well-mixed fluid, and second, a severe downslope windstorm is formed under the pool. Eventually, Kelvin-Helmholtz (KH) waves, which should also cause diapycnal mixing, emerge between the pool and the severe downslope windstorm. KH waves are instability waves growing in a shear flow that have an inflection point [*Drazin and Reid*, 1982], and they are often observed in the ocean and atmosphere.

In the ocean, *Afanasyev and Peltier* [2001] and *Lamb* [2004] performed vertically two-dimensional simulations of breaking, unsteady lee waves over the Knight Inlet sill with resolutions much finer than those of previous three-dimensional simulations of internal waves [e.g., *Legg*, 2004; *Ezer* et al., 2011] and breaking lee waves [e.g., *Nakamura et al.*, 2004]. *Afanasyev and Peltier* [2001] showed that a severe downslope windstorm is formed through a process similar to that in the atmosphere. *Lamb* [2004] showed that separation of the windstorm from the bottom occurs due to large-amplitude unsteady lee waves. Here, unsteady lee waves denote lee waves generated by a time-varying flow $U(x, t)$, a tidal flow in this case, and they consist of a superposition of waves with frequencies $-kU(x, t) \pm \omega$ excited at various positions and times, where k and ω are the horizontal wavenumber and the tidal frequency [*Nakamura et al.*, 2000].

However, the spatial resolutions of the ocean models of *Afanasyev and Peltier* [2001] and *Lamb* [2004] were still insufficient to resolve dynamical phenomena at spatial scales smaller than breaking, large-amplitude lee waves. Hence, these models did not reproduce the KH waves seen in simulations of the atmosphere, even though the simulated background flow was favorable for the development of KH waves. Moreover, transition processes in the ocean and atmosphere could differ because of differences in the solutions of steady and unsteady lee waves; the theoretical solution of unsteady lee waves for a nonlinear case is still unknown. Therefore, the transition processes to turbulence in the oceans are not sufficiently understood, even in two spatial dimensions. Moreover, the effects of transition processes such as the formation of KH waves and flow separation in diapycnal mixing have not been investigated; most previous studies focused on mixing by convection in statically unstable regions created by unsteady lee waves.

In this paper, we investigate transition processes to turbulence associated with a large-amplitude unsteady lee wave, and the effects of transition processes on mixing. Since transition processes produce turbulence, an understanding of the processes would contribute to a better understanding and estimation of mixing, which would lead to the improvement of parameterization schemes for diapycnal mixing that are required for ocean general circulation models. It is, however, difficult to investigate these processes by theoretical analysis or observation because of their strong nonlinearity and small spatiotemporal scales. Hence, we performed high-resolution numerical experiments using a nonhydrostatic vertically two-dimensional model.

Our numerical experiments treat the case of the Amchitka Pass in the Aleutian Passes (Fig. 1), where *Nakamura et al.* [2010] (henceforth, N10) observed the breaking of a large-amplitude unsteady lee wave with an amplitude of ~200 m. Although the case investigated is specific, the dynamics of the transition processes in this pass could be applicable to other regions. Indeed, we found that Tollmien-Schlichting (TS) waves are generated in the transition process and make a significant contribution to diapycnal mixing. TS waves are one kind of growing perturbation in viscous boundary layers [*Schlichting and Gersten*, 2000]. In oceanography, little attention has been paid to TS waves because of their small spatiotemporal scale, and there are no studies that suggest the possibility of TS wave excitation in the ocean.

In addition, the Amchitka Pass is an important site in the regional oceanography. The pass is a high-energy-dissipation region of the K_1 tide [*Egbert and Ray*, 2003] and the largest conduit for K_1 energy into the Bering Sea [*Foreman et al.*, 2006]. Mixing modifies the water in the pass, which flows into the North Pacific and the Bering Sea [e.g., *Reed and Stabeno*, 1993], and thus it affects material circulation and the ecosystem in the surrounding area [e.g., *Roden*, 1998]. In addition, mixing intensity may oscillate in association with the 18.6-year nodal cycle, which causes the tidal energy flux in the pass to vary by 36% [*Foreman et al.*, 2006]. This oscillation may be one factor in bi-decadal variations in water properties in the North Pacific and the Bering Sea [*Yasuda et al.*, 2006; *Osafune and Yasuda*, 2010].

The outline of this paper is as follows. In section 2, the numerical model is described. In section 3, the transition processes observed in the numerical simulation are presented, and then, a linear stability analysis to confirm the excitation of KH waves is conducted in section 4. The effects of the transition processes on mixing are discussed in section 5. The conclusions are summarized and discussed in section 6.

2. Numerical Model

The numerical model employed in this study was the vertically two-dimensional model of *Nakamura et al*. [2000]. The governing equations are the nonlinear and nonhydrostatic momentum equations for an incompressible Boussinesq fluid, the continuity equation, the advection-diffusion equations for potential temperature and salinity, and the equation of state [*UNESCO*, 1981]. The Coriolis parameter, *f*, was set to a constant value, 1.16×10^{-4} s^{-1}, at 51.58 °N. The model utilized the Arakawa scheme, which conserves both energy and enstrophy, and a third-order advection scheme for potential temperature and salinity.

The model topography is shown in Fig. 2, where the across-sill and vertical coordinates are denoted as *x* and *z*, respectively. The topography was determined from the observation data obtained by N10. The bottom topography consists of a two-dimensional mountain (sill) having two ridges and a valley between the ridges, and it is set to be flat on both sides of the sill with a maximum depth of 1100 m. This model topography represents the north-south section of an approximately two-dimensional ridge extending from west to east (Fig. 1(b)). Accordingly, unsteady lee waves develop quasi-two-dimensionally, although three-dimensional effects could be important in convection and breaking of KH and TS waves. Moreover, the transition processes are not well known even in vertically two-dimensional cases. Therefore, we consider vertically two-dimensional simulations as a reasonable first step toward a better understanding of transition processes in the ocean.

The horizontal and vertical grid sizes around the sill were 10 m and 1 m, respectively. The numbers of grid points in the horizontal and vertical directions were 1100 × 1100. The grid sizes are a few hundred times smaller than the spatial scales of large-amplitude lee waves generated over the sill. Thus, they are sufficient to explicitly resolve smaller scale dynamical instabilities causing small-scale turbulence.

The initial stratification was horizontally uniform, and was based on expendable conductivity temperature depth (XCTD) data obtained from the Pacific side of the Amchitka Pass in July 2007 during the T/S Oshoro-maru cruise. The stratification on the Pacific side is not significantly modified by tidal mixing in the pass because a weak mean flow crosses the pass from the North Pacific to the Bering Sea.

The forcing was a sinusoidal barotropic current across the sill with K_1 tidal frequency, and was introduced through the lateral boundaries of the model. Its maximum speed at the top of the higher ridge was set to be 55 cm s^{-1}, which is the value observed by N10. The flow across the sill was initially set to zero so that the transition processes can be observed clearly. The flow then started to travel to the right (i.e., from the North Pacific to the Bering Sea). The flow along the sill, *v*, was initialized as $v = f\sigma_f^{-1}\widehat{U}(x)$, where $\widehat{U}(x)$ is the amplitude of the barotropic flow across the sill and σ_f is its frequency.

To parameterize turbulent eddy mixing on the subgrid scale, the eddy viscosity and diffusivity coefficients used by *Nakamura et al*. [2000] were modified in this study. The horizontal eddy viscosity coefficients were represented by the sum of a background value (50 cm^2 s^{-1}) and values were calculated using a Smagorinsky-type model. The vertical component was set to be the larger of a background value (0.2 cm^2 s^{-1}), and the value, K_M, calculated using a level-two turbulence closure model, given by,

$$K_M = \sqrt{\frac{S}{C}} \cdot S|1 + \alpha R_{\mathrm{i}}|^{-\frac{1}{2}} l^2 \left[\left(\frac{\partial u}{\partial z}\right)^2 + \left(\frac{\partial v}{\partial z}\right)^2 + P_r^{-1}|N^2|\right],$$

$$R_i = N^2 / \left\{\frac{S}{C}\left[\left(\frac{\partial u}{\partial z}\right)^2 + \left(\frac{\partial v}{\partial z}\right)^2 - P_r^{-1}|N^2|\right]^2\right\},$$

where the constants were S = 0.39 and C = 0.06, which are the same as in the *Mellor and Yamada* [1982] model; the empirical coefficient α was set to be 120; R_i is the Richardson number; l is the length scale of the turbulence; u and v are the cross- and along-sill velocities, respectively; P_r is the Prantl number; and N is the Brunt-Väisälä frequency. This turbulence closure model is derived from *Noh and Kim's* [1999] level-2.5 turbulence closure model under the assumption that the sum of the shear production and the buoyancy terms is equal to the energy dissipation term. The background eddy viscosity coefficients are sufficiently small to demonstrate the transition processes. The eddy diffusivity coefficients are equal to the values of the eddy viscosity coefficients divided by P_r, where P_r was five. This value was employed both to reduce the effects of numerical dispersion by increasing the eddy viscosity coefficients and to better reproduce stirring processes of salinity and potential temperature by decreasing the eddy diffusivity coefficients. Changing P_r to 1 or 2 did not qualitatively alter the results.

At the bottom boundary, a no-slip condition was imposed in the sill region and a free-slip condition was imposed in the deep regions with flat bottoms. At the surface, a rigid-lid approximation was used, and no momentum, heat, or freshwater flux was assumed. An open boundary condition was applied at the lateral boundaries. The initial stratification was imposed at the inflow boundary, and an outflow condition was applied at the outflow boundary. Sponge regions were employed on both right and left sides to suppress artificial wave reflection. In the sponge regions, the background values of horizontal eddy viscosity and diffusivity coefficients were gradually increased up to 2.0×10^8 cm^2 s^{-1} and 4.0×10^7 cm^2 s^{-1}, respectively, near the lateral boundaries. The sponges occupied the first 150 grids and the last 150 grids. The horizontal grid size was also gradually increased near the lateral boundaries so that the sponges were sufficiently broad to prevent waves reflected at the lateral boundaries from coming to the sill.

The setup described above was used in the main experiment, referred to as experiment 1. In addition to this, experiments were performed with different setups (summarized in Table 1). Experiments 2 and 3 were performed to identify perturbations as TS waves, and experiments 4–12 were performed to examine the sensitivity for eddy viscosity coefficients. In the following sections, the results of experiment 1 will be described unless otherwise stated. In addition, to demonstrate the transition to turbulence, we will focus on the first half-cycle of the K_1 tide, during which the barotropic flow was directed from left to right. Dynamics of unsteady lee waves in the second half-cycle was similar to those in the first, although there were some differences due to the asymmetry of the topography and the presence of the unsteady lee waves generated in the previous half-cycle. For details of unsteady lee wave dynamics, refer to *Nakamura* et al. [2000].

3. Transition Processes

Diurnal tides are subinertial in the Amchitka pass, and hence unsteady lee waves were generated as internal waves, whereas diurnal internal tides cannot be internal waves [*Nakamura et al.*, 2000]. Breaking of large-amplitude unsteady lee wave occurred over the downslope in the lee of the higher ridge (henceforth, simply the downslope), and boundary layer separation occurred over the valley (Fig. 3). These processes were responsible for intense diapycnal mixing, as will be shown in section 5. We describe first the transition processes over the downslope, and then, those over the valley. Although wave breaking also occurred in the lee of the lower ridge, we will not include its description here because the wave amplitudes and mixing intensity were smaller than those observed in the lee of the higher ridge.

3.1. Over the Downslope

We found that the transition processes over the downslope can be divided roughly into three stages. Before each of these stages is considered in turn, the excitation of a large-amplitude unsteady lee wave is described.

As the barotropic flow accelerates, a large-amplitude unsteady lee wave (henceforth, simply an unsteady lee wave) with a ~1.5-km horizontal wavelength is excited over the downslope, as seen in the potential density (σ_θ) shown in Fig. 3(a). Co-phase lines are slanted to the upstream side (i.e., south) in both the current and density fields (Figs. 3(a) and 4(a)). This is a characteristic feature of lee waves. The ratio of lee wave frequency to tidal frequency, kU/ω, was estimated to exceed 14 (k and U were estimated from Fig. 3(a) and by depth averaging) over the downslope at the time of Fig. 3(a), suggesting that the wave is an unsteady lee wave [*Nakamura* et al., 2000].

The wave amplitude increases with time, and regions of potential static instability are observed (Fig. 3(b)). In addition, the unsteady lee wave moves downstream during the acceleration stage of the rightward flow (Figs. 3(a) to (c)). This is because the horizontal phase speeds of waves with various frequencies forming the unsteady lee wave are almost equal and in the opposite direction to the barotropic flow velocity at the time that the waves are excited [*Nakamura and Awaji*, 2001]. The advection of the unsteady lee wave influenced the location of boundary layer separation, as will be described in section 3.2.

3.1.1. First Stage

In the first stage of the transition, convection begins in the region of overturned isopycnals; in other words, wave breaking begins. Figs. 3(c) and (d) present the evolution of the potential density (σ_θ) field in this stage. In Fig. 3 (c), the wave height increases to ~200 m, and this value is comparable to that observed by N10 (Fig. 1(c)). The inverse Froude number ($\overline{N}\eta/U$) was estimated to exceed 1.7 over the downslope at the time of Fig. 3(c). Here, the wave height, η, was used instead of the topographic height because the tidal excursion was shorter than the topographic width. The value of the inverse Froude number implies that the wave generating force is sufficiently strong for the wave to break. The onset of wave breaking is earlier for the denser isopycnals than for the lighter, because the steepness of overturning isopycnals is larger for the denser isopycnals (Figs. 3(b) and (c)). This means that the region where convection occurs extends toward the top of the higher ridge. The spatial scales of the convection vary with isopycnal, and the horizontal scale ranges from 100 m to 300 m. The vertical scale also seems to vary; however, estimating variations in the vertical scale is difficult because they also depend on the growth of convection.

Unlike the breaking of a finite-amplitude steady lee wave investigated in previous studies, such as *Scinocca and Peltier* [1993], convection in our simulation occurs on both the upstream (left) and downstream (right) sides of the crest, as seen in the potential density (Fig. 3(c)) and velocity fields (Figs. 4(c) and 5) in the vicinity of the 26.6 σ_θ isopycnal, for example. Around the left side of the wave crest, the vertical velocity is downward to the right of the 26.6 σ_θ isopycnal (the dashed arrow on the left in Fig. 5). We call this type of wave breaking forward wave breaking. In the previous atmospheric study, only this type of breaking was identified. On the far right of the isopycnal, the fluid is advected to the upper right through the upper part of the wave crest (the solid arrows in Figs. 4(c) and 5), and thus becomes denser than the surrounding fluid. As a result, the fluid on the right side of the wave crest becomes statically unstable and then the denser fluid moves to the lower right (the right-hand dashed arrow in Fig. 5), that is, backward wave breaking begins. Similar forward and backward wave breaking also occurs near other isopycnals.

To the best of our knowledge, this is the first study to report backward wave breaking of unsteady lee waves, and the phenomenon is yet to be observed. This type of wave breaking is not expected in linear or nonlinear theories of atmospheric lee waves. According to the lee wave theories, crests of lee waves grow along phase lines tilting upstream, and hence, only forward wave breaking can occur. Interestingly, backward wave breaking also occurred in our simulation, suggesting the presence of a missing factor in the mechanism of wave breaking in the oceans. Moreover, the occurrence of backward wave breaking in addition to forward wave breaking should make the mixing area wider than that in the case of forward wave breaking alone. Therefore, backward wave breaking would also enhance diapycnal mixing.

A strong rightward flow develops near the sea surface directly above the regions of backward breaking (Fig. 4(b)). This flow strengthens with time (Figs. 4(b) to (d)) and is sustained until the barotropic flow ceases. A similar surface flow was observed by N10 (Fig. 1(d)). In addition, another rightward flow develops over the wave crest on the 26.7 σ_θ isopycnal (Fig. 4(c)), which shows backward breaking. These rightward flows and the backward wave breaking occur quite near each other, suggesting a close relationship between these phenomena. Clarification of this relationship and of the cause of backward wave breaking needs to be investigated further.

Under the statically unstable region in which convection occurs, a downslope flow develops as the unsteady lee wave grows. Fig. 6 shows a Hovmöller diagram of the baroclinic across-sill velocity 30 m above the bottom, where the maximum downslope flow speed occurs in the vertical direction. Here, the baroclinic velocity is defined as the difference of the simulated velocity and the barotropic component (the depth-averaged flow). The speed of downslope flow increases with time, and after the barotropic flow accelerates to its maximum speed (i.e., after 0.25 period), the downslope flow becomes fully developed (Fig. 6). This state corresponds to the severe downslope windstorm observed in previous studies [e.g., *Laprise and Peltier,* 1989]. Together with the unsteady lee wave, the downslope flow enhanced shear, which lead to the phenomena in the next stage.

3.1.2. Second Stage

In the second stage of the transition, finite-amplitude perturbations develop in a strong shear region between the convective mixing region and the downslope flow, and their growth process is shown in Fig. 7. These perturbations are expected to be KH waves; this expectation will be confirmed in section 4, using a one-dimensional linear stability analysis.

Finite-amplitude KH waves of two wavelengths emerge (indicated by arrows in Fig. 7(a)) and propagate downstream with increasing amplitude (Figs. 7(a) to (c)). The propagation is also seen in the Hovmöller diagram (Fig. 6). Phase speeds and wavelengths of the KH waves estimated from Fig. 6 ranged from 35 to 50 cm s^{-1} and from 450 to 500 m, respectively. Hence, their frequencies were 4.9–6.3 × 10^{-3} rad s^{-1}, which are much higher than diurnal tidal frequencies (≈ 7.3 × 10^{-5} rad s^{-1}). Note that the phase speed varied with time because it depends on the background flow, which varied temporally.

As the amplitude of KH waves increases with time, well-defined KH billows with positive vorticity appear around 0.8-km distance and 170-m above the bottom (Figs. 7(d) and 8). Animation of the numerical results (not shown) demonstrated that the fluid forming the KH billows came not from the downstream region but from the downslope flow. The KH billows continue to occur in the third stage. Note that the spatial scale of the simulated KH waves is as small as or smaller than the observation intervals (approximately 500 m) of N10 (Fig. 1(c)). Hence, it is difficult to confirm that KH waves were present during the observation. The same can be said for dynamical phenomena with spatial scales similar to or smaller than KH waves.

3.1.3. Third Stage

The third stage is characterized by the growth and subsequent modification of finite-amplitude perturbations that appear in the bottom boundary layer (BBL) under the KH billows (Fig. 9) and have horizontal scales similar to the KH billows. These perturbations are identified as TS waves. In fact, a characteristic feature of TS waves is seen in the simulated vertical velocity field; as shown by the dashed curve in Fig. 10, the phase lines of vertical velocity tilt in the opposite direction to the background flow close to the bottom boundary and are vertical at finite distances from the bottom [*Baines et al*, 1996]. Moreover, these perturbations were not seen in the experiment with a free-slip condition at the sill (experiment 2) because bottom stress is one of the necessary conditions for TS waves. Although the TS waves seem to correspond to the wavelength of perturbations in the topography in Fig. 9(a), TS waves were also excited without the undulation of topography (experiment 3), as shown in Fig. 11, indicating that the topographic undulation was not an essential factor.

Propagation of the TS waves is observed as the movement of positive and negative velocity perturbations in Fig. 6. The phase speed estimated from Fig. 6 was 23 cm s^{-1}, which was similar to the propagation speed of the KH billows in this stage. The frequency was 2.9×10^{-3} rad s^{-1}, which is much higher than diurnal tidal frequencies.

The TS waves grow to form vortices on the bottom and their vertical scale increases to approximately 50 m (Fig. 9(b)). The vortices stretch vertically and break down as they move slowly downstream (Fig. 9(c)). Significant fractions of the breaking vortices are carried into the statically unstable region by both the breaking unsteady lee wave and the KH waves, and other fractions move down to the valley. The movement of the former fractions results in the entrainment of dense water into the statically unstable region. The formation and breakdown of the vortices were repeated until the barotropic flow ceased. These results suggest that TS waves can contribute significantly to diapycnal mixing, as will be discussed in section 5.

3.2. Over the Valley

Before the unsteady lee wave breaks, the downslope flow separates from the bottom boundary near 1.6-km distance, and a reverse flow forms under the separated flow (Figs. 3(a) and 4(a)). This boundary layer separation was due to the adverse pressure gradient created by the unsteady lee wave. *Lamb* [2004] explained flow separation associated with unsteady lee waves in his simulation as post-wave separation defined by *Baines* [1995], which is controlled by both upstream blocking and the adverse pressure gradient created by unsteady lee waves. In our simulation, however, upstream blocking was absent. Therefore, our flow separation is different from this type of post-wave separation.

The separated flow rolls up and sheds vortices quasi-periodically (Figs. 3, 7 and 9). Vortices continue to be shed but become smaller after 0.3 period (Figs. 7(d) and 9). Most vortices merge with adjacent vortices in pairs, stretch vertically, and eventually break (Figs. 3(c) and (d), 7 and 9). As a result, strong stirring and thus mixing occur downstream of the vortex shedding point. Vortex shedding and pairing are essentially three-dimensional phenomena and the details are beyond the scope of this study.

The flow separation point and vortex shedding point move down in the lee of the ridge (Figs. 3(a) to (c)) as the unsteady lee wave is advected downstream by the background flow. After the barotropic flow velocity reaches a maximum, both flow separation point and vortex shedding point stay around a 3.0-km distance until breaking vortices associated with TS waves reach the shedding point (Figs. 3(c) and (d), 7, and 9(a) and (b)). The movement of the separation point is also roughly seen in Fig. 6 as movement of the starting point of the reverse flow. Note that this correspondence is not exact because Fig. 6 does not show the bottom velocity (actually 30 m above the bottom) because the barotropic component is subtracted.

4. Linear Stability Analysis

This section describes a one-dimensional linear analysis, which was conducted to examine whether the perturbations in the second stage of the transition over the downslope (section 3.1.2.) are KH waves. In the analysis, the background flow was approximated to be horizontally parallel. This approximation should be reasonable for investigating the essential dynamics, given that the structure of the background flow profile varied sufficiently slowly with time and horizontal distance, and that the variations in the bottom depth were not sufficiently large to alter the dynamics of KH waves. We ignored the Coriolis term, viscosity, and diffusivity, which are not important on the spatial scales of the simulated KH waves.

The linear stability of an inviscid and non-diffusive stratified shear flow, $\bar{u}(z)$, to two-dimensional perturbations is determined by the solutions of the Taylor–Goldstein equation [*Drazin and Reid*, 1981],

$$\frac{d^2\varphi}{dz^2} + \left[\frac{N^2}{(\bar{u}-c)^2} - k^2 - \frac{\frac{d^2\bar{u}}{dz^2}}{(\bar{u}-c)}\right]\varphi = 0, \qquad (1)$$

which is derived from the linearized momentum equations for the *x*- and *z*-directions, the continuity equation, and the advection equation for density. Here, the stream function of the perturbation is defined as $\psi'(x, z, t) = \varphi(z)\exp[ik(x-ct)]$ and is related to the perturbation velocity in the *x*- and *z*-directions through $u = -\partial\psi'/\partial z$ and $w = \partial\psi'/\partial x$, respectively; k is the real wavenumber in the *x*-direction; $c = c_r + ic_i$ is the complex phase speed governing linear stability. At the top (z = 0) and bottom boundaries, $\varphi(z)$ was set to be zero, and a free-slip condition was imposed. Numerical solutions of (1) were obtained using a shooting method (i.e., we integrated (1) with the fourth-order Runge-Kutta method from z = 0 to the bottom boundary, and searched for the solution that satisfies the boundary conditions by iteration, using the code provided by *Brankin and Gladwell* [1997]).

Fig. 12 shows vertical profiles of the background stratification and flow, which were taken at 1.1-km distance at 0.266 period (dashed line in Fig. 4(d)), just before KH waves appear. Small disturbances such as convection were excluded from the profiles using a multi-term approximation. Because effects of viscosity and diffusivity are significant in the BBL, we excluded the BBL from the background flow in this analysis, where the BBL is defined as the layer between the bottom and the depth of the maximum downslope flow speed in the vertical direction (30 m above the bottom).

As expected, the results of the analysis showed the presence of growing modes, whose phase speed and growth rate are shown in Fig. 13(a). The phase speed varies with wavenumber in Fig. 13(a), owing to the vertical asymmetry of the background flow profile [*Hazel*, 1972]. Phase speeds are approximately 40 cm s^{-1} for modes with horizontal wavelengths of the perturbations that are dominant in the simulation (450–500 m, corresponding to wavenumbers of 0.0126–0.0140). This speed is almost equal to the estimated phase speeds in the simulation.

Growth rates for the wavelengths of the simulated perturbations are roughly 1.0×10^{-3} s^{-1} (Fig. 13(a)) and are large enough for perturbations to grow during the first half of the second stage (0.05 period), although the wavelengths in the simulation were somewhat different from those of the fastest growing mode (630 m). This difference in wavelength could be a result of the spatiotemporal variability of the background flow neglected in the analysis. In the simulation, the growth rate was approximately 4.6×10^{-3} s^{-1}, which was estimated from the variability of wave heights between 0.290 and 0.299 period (Figs. 7(a) to (c)). The difference in growth rate between the analysis and the simulation may be caused as a result of convection, which seeded disturbances in the simulated shear flow.

A perturbation stream function is shown in Fig. 13(b) for a wavelength of 500 m (a wavenumber of 0.0126). The structure shown was typical for a wide range of wavenumbers (0.006–0.015), which encompasses the wavenumbers realized in the simulation. The stream lines form a closed cell centered at a depth of 170 m and extending between the depths of the maximum and minimum background velocity. The depth of the cell is almost the same as that of the simulated KH billows that emerged in the simulation results (Figs. 7(d) and 8).The cell with negative perturbation vorticity seen in the analysis is less visible in the simulation due to superposition of the background flow.

The above analysis shows that major features of the instability are consistent with those in the simulation, although there are some differences between the analysis and simulation results. However, it is still difficult to identify whether the perturbations are KH or Holmboe modes [*Holmboe*, 1962]; for the former modes, shear is more important than stratification, and for the latter the converse holds [*Winters and Riley*, 1992]. Thus, we also analyzed the same flow but with no stratification (i.e., $N^2 = 0$). The results are shown in Figs. 13(c) and (d). The horizontal phase speed and the structure of the perturbation stream function are quite similar to those of the stratified fluid case for the same wavenumber (0.0126). These similarities between the two cases indicate that shear effects are dominant for the mode found in the stratified fluid case. Moreover, the growth rates in all wavelength ranges are higher than the growth rates in the case of stratified fluid, indicating that the stratification acted to stabilize the flow. Therefore, the modes in the stratified fluid case and hence the simulated perturbations are regarded as a KH mode.

5. Effects on Mixing

The evolution of the potential density field (Figs. 3, 7, and 9) described in section 3 suggests that KH and TS waves and boundary layer separation enhance diapycnal mixing, as well as convection caused by density inversions induced by an unsteady lee wave. In this section, we qualitatively examine their role in diapycnal mixing using two measures.

The first is the density variance dissipation rate χ_ρ. This measure was employed to focus on stirring resolved in the simulations, which is thus determined by the momentum and advection-diffusion equations and is not affected directly by the subgrid-scale mixing parameterization. The definition of χ_ρ has the same form as the temperature variance dissipation rate, namely,

$$\chi_\rho = 2c_0\left[\left(\frac{\partial\rho'}{\partial x}\right)^2 + \left(\frac{\partial\rho'}{\partial z}\right)^2\right].$$

In the following analysis, c_0 was set to one, and ρ' was the potential density after the application of a high-pass filter in the vertical direction using a Lanczos filter with 41 weights and a cut-off wavelength of 10 m. Accordingly, χ_ρ represents the magnitude of the density gradient caused by resolved small perturbations, thus, χ_ρ is a measure of resolved stirrings. Because strong stirring easily leads to mixing in the presence of diffusion, χ_ρ relates to effects on mixing. Note that varying the cut-off wavelength within a range of 5–20 m did not produce a qualitative difference. In addition, the influence of numerical noise was confirmed to be negligible by comparison with the results obtained by using a band-pass filter with a range of 5 to 10 m in the calculation of ρ'.

Spatial distributions of χ_ρ illustrate regions of enhanced stirring or mixing (Fig. 14). In the first stage over the downslope, values of χ_ρ initially increase in regions where convection occurs (Figs. 14(b) to (d)). In the second and early third stages (after KH waves and billows develop, until TS waves emerge), areas of enhanced χ_ρ spread to near the sea surface and to 100 m above the bottom over the downslope (Figs. 14(e) to (i)). In particular, χ_ρ becomes high near the top and bottom of the statically unstable region. When vortices associated with TS waves develop (in the latter half of the third stage), χ_ρ becomes high in the KH billows over the TS waves (Fig. 14(j)). After the vortices begin to break, high χ_ρ values also appear in the region where fractions of broken vortices are entrained into the statically unstable region (Fig. 14(k)).

Over the valley, the high χ_ρ regions extend to near the sea surface associated with the formation and shedding of vortices and with the stretching and merging of shed vortices (Fig. 14). In particular, values of χ_ρ are high around breaking shed vortices.

The temporal evolution of the area-averaged χ_ρ ($<\chi_\rho>$) is shown in Fig. 15 (thick line). The area average was conducted separately for the two regions over the downslope and the valley, because dynamical processes that enhance mixing are different in these regions. Over the downslope, $<\chi_\rho>$ is roughly constant in the early phase of development of the unsteady lee wave (Fig. 15(a)). It then increases exponentially as vortex formation and shedding associated with the boundary layer separation start, because in the early stage boundary layer separation occurred over the downslope. Although convection increases $<\chi_\rho>$ after its onset, $<\chi_\rho>$ is almost constant for a short time, because the increase due to convection is negated by the decrease due to the movement of both the shed vortices and the shedding point to outside of the area-averaged region. An exponential increase starts again with the convection and KH wave excitation. The value of $<\chi_\rho>$ reaches a local maximum as the KH billows become well defined.

As TS waves are excited and formed vortices, which subsequently break down, $<\chi_\rho>$ increases gradually with some variation. The variation is caused by in- and out-flow of high χ_ρ water across the lateral boundaries of the area-averaged region. Then, $<\chi_\rho>$ reaches its peak value and remains high. This peak is attributed to the breakdown of vortices of TS-wave origin and to KH billows dominant in the statically unstable region. In the experiment with a free-slip condition at the sill (experiment 2), TS waves were not excited and $<\chi_\rho>$ decreased after the peak associated with KH billows (not shown). This is different from the experiment with a no-slip condition, indicating that TS waves and associated vortex formation enhance mixing.

Over the valley, the increase of $<\chi_\rho>$ consists of two steps (Fig. 15(b)). The first increase begins as flow separation and vortex shedding occur. The increase continues due to expansion of areas where breakdown of shed vortices occur. After the expansion stops, $<\chi_\rho>$ becomes nearly constant. The second increase results from the reduction in size of shed vortices. Reduction in vortex size leads to an increase in area of high density gradient, which occurs in the fringes of breaking vortices (Figs. 7(d) and 9). As a result, the value of $<\chi_\rho>$ increases and remains high until the barotropic flow ceases.

The second measure is the rate of the change of the background potential energy due to diapycnal mixing, Φ_d [*Winters* et al., 1995]. This measure represents effects of diapycnal mixing due to both resolved motions and subgrid-scale diffusion and is defined as

$$\Phi_d = g \int_V -\frac{dz_*}{d\rho}\left[\kappa_H \left(\frac{\partial \rho}{\partial x}\right)^2 + \kappa_Z \left(\frac{\partial \rho}{\partial z}\right)^2\right] dV,$$

where g is the acceleration due to gravity; V, the integration volume; $\rho(\boldsymbol{x}, t)$, the potential density; and $z_*(\rho)$, the vertical position in the reference state of the minimum potential energy obtained by sorting the volume elements by density; further, κ_H and κ_Z are the horizontal and vertical eddy diffusivity coefficients, respectively. As shown in Fig. 15, the temporal evolutions of Φ_d and $<\chi_\rho>$ are similar to each other. This similarity comes from the fact that both measures include the square of the space derivative of the potential density, and it shows that high χ_ρ values are related to strong mixing in the present case. Thus, although the subgrid-scale diffusion is affected by the parameterization method, the conclusions are robust to each measure.

The above analysis results indicate that convection, the development of KH and TS waves, and boundary layer separation extend regions of enhanced mixing from near the sea surface to near the bottom and increase the area-averaged mixing intensity. Therefore, we conclude that diapycnal mixing can be enhanced not only by convection but also by other dynamical phenomena involved in the transition processes.

6. Conclusions and Discussion

In the present study, we have investigated the processes associated with the breaking of large-amplitude unsteady lee waves, i.e., the processes of transition to turbulence, using a vertically two-dimensional nonhydrostatic model with realistic topography of the Amchitka Pass. Our high-resolution simulation showed that over the downslope in the lee of the higher ridge, the transition process proceeded in three stages. In the first stage, convection occurred in a density inversion region created by a mature large-amplitude unsteady lee wave; in other words, wave breaking started. Breaking of the unsteady lee wave occurred on the upstream side (forward wave breaking) and the downstream side of the wave crest (backward wave breaking). Below the breaking unsteady lee wave, downslope flow accelerated and matured. The mature state corresponds to the severe downslope windstorms reported in previous studies [*Scinocca and Peltier*, 1993; *Afanasyev and Peltier*, 2001]. In the second stage, finite-amplitude KH waves were generated in a strong shear region between the statically unstable region and the downslope flow, and these waves grew to form KH billows. In the third stage, TS waves developed in the BBL and grew to form vortices, which eventually broke down. Over the valley, downstream of the higher ridge, the downslope flow separated from the bottom boundary. The separated shear layer formed vortices and vortex shedding occurred, resulting in intense mixing. To the best of our knowledge, this is the first study reporting backward wave breaking of unsteady lee waves and the excitation of oceanic TS waves.

The development of KH and TS waves and boundary layer separation enhanced diapycnal mixing as well as convection caused by density inversions of a large-amplitude unsteady lee wave. Note that KH and TS waves obtain their energy from the kinetic energy of the background flow, in contrast to convection whose energy source is the potential energy of the lee wave. This difference in energy source has an important implication: the development of these waves affects the total amount of energy transferred to turbulence at the generation sites of lee waves.

In regions where N10 and *Legg and Klymak* [2008] expected the excitation of large-amplitude lee waves, intense diapycnal mixing may occur through transitions similar to those we have reported in this paper, if the necessary conditions for KH and TS waves are satisfied. The necessary conditions for KH waves would be met if unsteady lee waves or downslope flow have sufficient growth such that the shear has an inflection point and *Ri*, the ratio of stratification to shear, is less than a quarter. For TS waves, the necessary conditions are (1) the presence of bottom stress, (2) the presence of BBLs, and (3) that the Reynolds numbers, the ratios of inertia to viscosity, of the BBLs are in the range at which TS waves are unstable. The unstable range depends on velocity profiles within the BBLs. In real oceans, there is a possibility of TS waves being excited, as at least bottom stress and the presence of BBLs are satisfied. However, observations of TS waves in the ocean are needed to verify this.

Simulation results, particularly small-scale phenomena such as KH and TS waves, would be affected by eddy viscosity and grid resolution. First, we examine the influence of the turbulence closure model used in our simulation on KH and TS waves. Turbulence closure schemes affect the spatiotemporal variation and magnitude of eddy viscosity. In general, viscosity is large in a BBL where TS waves could develop, whereas it is small in the interior region where KH waves could develop. Because viscous force is important for TS waves but works against KH waves, large and small viscosities tend to be favorable for TS and KH waves, respectively. Therefore, the use of a turbulence closure model would facilitate the development of both kinds of waves. To investigate the influence of spatiotemporal variation and the magnitude of eddy viscosity caused by the turbulence closure model used in experiment 1, nine sensitivity experiments were performed with constant eddy viscosity coefficients. The setup and results of the experiments are summarized in Table 2. In experiments 4–9, the magnitude of viscosity coefficient was varied while keeping the ratio of horizontal and vertical eddy viscosity coefficients fixed, but in experiments 10–12, viscosity coefficients were determined based on the results of experiment 1. KH waves occurred in all the experiments, and TS waves appeared in experiments 8 and 11. Note that wavelengths of the KH and TS waves were different from those of experiment 1 because of a difference in flow profile between the experiments. TS waves did not appear in the other experiments (4–7, 9, 10, and 12) because a too-large vertical viscosity damped TS waves or because a too-small vertical viscosity made the BBL too thin (less than 10 m) to resolve TS waves. Although TS waves are somewhat sensitive to the magnitude of viscosity, the occurrence of KH and TS waves with constant viscosity coefficients suggests that the excitation of KH and TS waves does not require spatiotemporal variation of viscosity coefficients and therefore the turbulence closure model.

Next, the influence of grid resolution is considered. In experiment 1, KH waves were resolved by ~50 grids in a horizontal wavelength. For TS waves, the viscous response, i.e., the tilting of phase lines, was resolved by ~20 grids in the vertical direction. Therefore, the grid resolution is sufficient or reasonable for KH and TS waves. Nevertheless, if the resolution was increased, simulation results could be quantitatively altered for TS waves; their growth rate, for example, could be affected. Conversely, with insufficient resolution, KH and TS waves would not be excited.

Stratification became weaker with time due to diapycnal mixing caused by the transition processes. Weakening of stratification would affect the generation and properties of unsteady lee waves. The waves, nevertheless, were excited and broke again in the next tidal cycle. KH and TS waves also developed because stratification effects were sufficiently small, particularly in the wave-breaking region. Moreover, a mean northward flow is present in the region we focused on, and, although the northward flow is much slower than the tidal flow [e.g., *Reed and Stabeno*, 1993], the water mass modified by mixing would be advected away by the mean flow. Thus, restratification would occur. Therefore, the transition processes discussed in this paper would occur repeatedly even if mixing acts to weaken the stratification.

We employed the density variance dissipation rate and the rate of the change of the background potential energy due to diapycnal mixing. Diapycnal mixing strength, however, is often investigated using two other measures: the Thorpe scale, L_T, [*Thorpe*, 1977] and the dissipation rate of kinetic energy. However, there are some difficulties in applying these measures in the present case. First, the method using L_T are often employed to indirectly estimate eddy diffusivity coefficients. It has not been confirmed, however, that the Thorpe scale method is applicable when L_T is of the order of 100 m or more [*Wesson and Gregg*, 1994]. In the present simulations, inversions with L_T exceeding 100 m were abundant in the lee of the higher ridge. Furthermore, L_Ts were determined not by one vortex but by the combination of several vortices in our results. It follows that L_T did not represent the vertical size of the largest eddies, that is, the relationship of L_T and the Ozmidov length scale [*Ozmidov*, 1965] was unclear. Thus, it is not known whether the method is applicable to our simulation results. Second, the energy dissipation rate is often calculated by replacing the molecular viscosity coefficients with the eddy viscosity coefficients. However, the physical meaning of the energy dissipation rate estimated by this method is not completely clear because the eddy viscosity coefficient depends on a parameterization used for subgrid-scale mixing that also has a role in reducing numerical noise and because it does not represent all dissipation taking place in the model (numerical diffusion is not accounted for).

For the above reasons, we focused on the density variance dissipation rate, which is the measure of stirring due to resolved motions in the present definition. Actually, the result of the density variance dissipation rate was similar to that of the rate of the change of the background potential energy due to diapycnal mixing, which includes the effects of the subgrid-scale parameterization. Accordingly, the qualitative results are robust to the subgrid-scale mixing parameterization used here, suggesting that the energy dissipation rate would also yield qualitatively similar results if the conversion from kinetic to potential energy was represented adequately in the model.

Some points such as the mechanism of backward wave breaking and the relationship between backward wave breaking and strong sea-surface flow remain to be clarified. In addition, three-dimensional simulations are required for a complete understanding of the transitions, because convection, KH billows, and vortices induced by growing TS waves have three-dimensional structures in mature phases. From an oceanographic perspective, a quantitative estimate of diapycnal mixing in the Amchitka Pass is necessary for examining the relative importance of the transition processes in modifying water mass properties in the surrounding region. These points need to be investigated in the future.

Acknowledgments

The authors thank the anonymous reviewers for their useful comments. S.A. was supported by a Grant-in-Aid for JSPS Fellows, and T.N. was supported by KAKENHIs and JHPCN. Numerical calculations and analyses were done on the SR11000 or SR16000 at IIC Hokkaido University and on the PORC information system at ILTS Hokkaido University.

References

Afanasyev, Y. D., and W. R. Peltier (2001), On breaking internal waves over the sill in Knight

Inlet, *Proc. R. Soc. A*, *457*, 2799–2825, doi: 10.1098/rspa.2000.0735.

Baines, P. G. (1995), *Topographic Effects in Stratified Flows*, Cambridge Univ. Press, New York.

Baines, P. G., S. J. Majumdar, and H. Mitsudera (1996), The mechanics of the Tollmien-Schlichting wave, *J. Fluid Mech.*, *312*, 107–124, doi: 10.1017/S0022112096001930.

Brankin, R.W., and I. Gladwell (1997), Algorithm 771: rksuite_90: Fortran 90 software for ordinary differential equation initial-value problems, *ACM Trans. Math. Softw.*, *23*, 402–415.

Drazin, P. G., and W. H. Reid (1981), *Hydrodynamic Stability*, Cambridge Univ. Press, New York.

Egbert, G. D., and R. D. Ray (2003), Semi-diurnal and diurnal tidal dissipation from TOPEX/Poseidon altimetry, *Geophys. Res. Lett.*, *30*(17), 1907, doi:10.1029/2003GL017676.

Ezer, T., W. D. Heyman, C. Houser and B. Kjerfve (2011), Modeling and observations of high-frequency flow variability and internal waves at a Caribbean reef spawning aggregation site. *Ocean Dyn.*, 61(5), 581–598, doi: 10.1007/s10236-010-0367-2.

Farmer, D. M., and H. J. Freeland (1983), The physical oceanography of fjords, *Prog. Oceanogr.*, *12*, 147–219, doi: 10.1016/0079-6611(83)90004-6.

Foreman, M. G. G., P. F. Cummins, J. Y. Cherniawsky, and P. Stabeno (2006), Tidal energy in the Bering Sea, *J. Mar. Res.*, *64*, 797–818, doi:10.1357/002224006779698341.

Hazel, P. (1972), Numerical studies of the stability of inviscid stratified shear flows, *J. Fluid*

Mech., *51*, 39–61, doi:10.1017/S0022112072001065.

Holmboe, J. (1962), On the behavior of symmetric waves in stratified shear layers, *Geophys. Publ.*, *24*, 67–113.

Klymak, J. M., R. Pinkel, and L. Rainville (2008), Direct breaking of the internal tide near topography: Kaena Ridge, Hawaii, *J. Phys. Oceanogr.*, *38*, 380–399, doi: 10.1175/2007JPO3728.

Lamb, K. G. (2004), On boundary-layer separation and internal wave generation at the Knight Inlet sill, *Proc. R. Soc. A*, *460*, 2305–2337, doi: 10.1098/rspa.2003.1276.

Laprise, R., and W.R. Peltier (1989), The linear stability of nonlinear mountain waves: Implications for the understanding of severe downslope windstorms, *J. Atmos. Sci*., *46*, 545–564.

Legg, S. (2004), Internal Tides Generated on a Corrugated Continental Slope. Part I: Cross-Slope Barotropic Forcing. *J. Phys. Oceanogr.*, *34*, 156-173, doi: 10.1175/1520-0485(2004).

Legg, S., and J. Klymak (2008), Internal hydraulic jumps and overturning generated by tidal flow over a tall steep ridge, *J. Phys. Oceanogr.*, *38*, 1949–1964, doi:10.1175/2008JPO3777.1.

Long, R. R. (1953), Some aspects of the flow of stratified fluids. I. A theoretical investigation, *Tellus*, *5*, 42–58.

Mellor, G. L., and T. Yamada (1982), Development of a turbulent closure model for geophysical fluid problems. *Rev. Geophys.*, 20, 851–875, doi: 10.1029/RG020i004p00851.

Munk, W., and C. Wunsch (1998), Abyssal recipes II: Energetics of tidal and wind mixing, *Deep*

Sea Res. Part I, *45*(12), 1977–2010, doi:10.1016/S0967-0637(98)00070-3.

Nakamura, T., and T. Awaji (2001), A growth mechanism for topographic internal waves generated by an oscillatory flow, *J. Phys. Oceanogr.*, *31*, 2511–2524, doi: 10.1175/1520-0485(2001)031<2511:AGMFTI>2.0.CO;2.

Nakamura, T., and T. Awaji (2004), Tidally induced diapycnal mixing in the Kuril Straits and its role in water transformation and transport: A three-dimensional nonhydrostatic model experiment, *J. Geophys. Res.*, 109, C09S07, doi:10.1029/2003JC001850.

Nakamura, T., T. Awaji, T. Hatayama, K. Akitomo, T. Takizawa, T. Kono, Y. Kawasaki, and M. Fukasawa (2000), The generation of large-amplitude unsteady lee waves by subinertial K_1 tidal flow: A possible vertical mixing mechanism in the Kuril Straits, *J. Phys. Oceanogr.*, *30*, 1601–1621, doi:10.1175/1520-0485(2000)030<1601:TGOLAU>2.0.CO;2.

Nakamura, T., Y. Isoda, H. Mitsudera, S. Takagi, and M. Nagasawa (2010), Breaking of unsteady lee waves generated by diurnal tides, *Geophys. Res. Lett.*, *37*, L04602, doi:10.1029/2009GL041456.

Nash, J. D., M. H. Alford, E. Kunze, K. Martini, and S. Kelly (2007), Hotspots of deep ocean mixing on the Oregon continental slope, *Geophys. Res. Lett.*, *34*, L01605, doi:10.1029/2006GL028170.

Noh, Y., and H. J. Kim (1999), Simulations of temperature and turbulence structure of the oceanic boundary layer with the improved nearsurface process. *J. Geophys. Res.*, 104, 15621–15634, doi: 10.1029/1999JC900068.

Osafune, S., and I. Yasuda (2010), Bidecadal variability in the Bering Sea and the relation with 18.6 year period nodal tidal cycle, *J. Geophys. Res.*, *115*, C02014, doi: 10.1029/2008JC005110.

Ozmidov, R. V. (1965), On the turbulent exchangein a stablys tratifiedo cean, *Izv. Acad. Sci. USSR Atmos. Oceanic Phys.*, Engl. Transl., no. 1, 853–860.

Reed, R. K., and P. J. Stabeno (1993), The recent return of the Alaskan Stream to Near Strait, *J. Mar. Res.*, *51*, 515–527, doi:10.1357/0022240933224025.

Roden, G. I. (1998), Upper ocean thermohaline, oxygen, nutrients, and flow structure near the date line in the summer of 1993, *J. Geophys. Res.*, *103*, 12919–12940, doi: 10.1029/97JC03759.

Scinocca, J. F., and W. R. Peltier (1993), The instability of Long’s stationary solution and the evolution toward severe downslope windstorm flow. Part I: Nested grid numerical simulations, *J. Atmos. Sci.*, *50*, 2245–2263, doi: 10.1175/1520-0469(1993).

Schlichting, H., and K. Gersten (2000), *Boundary Layer Theory*, eighth ed. Springer-Verlag, Berlin, Heidelberg, New York.

Thorpe, S. A. (1977), Turbulence and mixing in a Scottish loch, *Philos. Trans. R. Soc. London, Ser. A*, *286*, 125–181, doi:10.1098/rsta.1977.0112.

UNESCO (1981), Tenth report of the joint panel on oceanographic tables and standards, *UNESCO Tech. Pap. Mar. Sci.*, *36*, Paris.

Wesson, J. C., and M. C. Gregg (1994), Mixing at Camarinal Sill in the Strait of Gibraltar, *J. Geophys. Res.*, *99*, 9847–9878, doi:10.1029/94JC00256.

Winters, K. B., and J. Riley (1992), Instability of internal waves near a critical level, *Dyn. Atmos. Oceans*, *16*, 249-278, doi: 10.1016/0377-0265(92)90009-I.

Winters, K. B., P. N. Lombard, J. J. Riley, E. A. D'Asaro (1995), Available potential energy and mixing in density-stratified fluids, *J. Fluid Mech.*, *289*, 115-128, doi: 10.1017/S002211209500125X.

Yasuda, I., S. Osafune, and H. Tatebe (2006), Possible explanation linking 18.6-year period nodal tidal cycle with bi-decadal variations of ocean and climate in the North Pacific, *Geophys. Res. Lett.*, *33*, L08606, doi:10.1029/2005GL025237.

Captions

Figure 1. Locations and results of observations by *Nakamura et al*. [2010]. (a) Location and (b) bottom topography of the Amchitka Pass. The red bar in panel (b) indicates the location of the observation sites in the Pass. (c) Cross-ridge (northward) baroclinic currents (the deviation from the

vertically averaged flow over the ridge top) and the horizontal resolution of the temporally averaged ADCP data (∇). Selected isotherms are superimposed. (d) Cross-ridge section of potential density and the XCTD (◊) sites. Arrows show the direction of barotropic cross-ridge flow at the ridge top.

Figure 2. Model topography (white) and initial stratification (color). Shadowed areas are sponge regions. Regions A, B, C, and D represent the areas shown in Figs. 3, 7, and 9; Figs. 4 and 8; Fig. 5; and Fig. 10, respectively.

Figure 3. The evolution of potential density (σ_θ) for experiment 1 around the sill top (region A in Fig. 2) during the first stage (beginning of breaking of a large-amplitude unsteady lee wave and boundary layer separation) at (a) 0.142, (b) 0.181, (c) 0.239, and (d) 0.266 K_1 period.

Figure 4. The evolution of the across-sill component of the velocity (cm s^{-1}) with potential density contours for experiment 1 over the down slope (region B in Fig. 2) at (a) 0.142, (b) 0.181, (c) 0.239, and (d) 0.266 K_1 period. The contour interval is 0.1 σ_θ. The arrow in panel (c) shows the rightward flow that causes backward wave breaking. The dashed line in panel (d) indicates the vertical section used in the linear stability analysis in section 4.

Figure 5. Vertical velocity (cm s^{-1}) with potential density contours focusing on region C in Fig. 4(c),

which corresponds to region C in Fig. 2. The contour interval is 0.1 σ_θ. The solid and dashed arrows show the vertical motion associated with forward and backward wave breaking, respectively.

Figure 6. Hovmöller plots of baroclinic across-sill velocity (cm s^{-1}) for experiment 1 at 30 m above the bottom around the sill top during the first half period. Baroclinic velocity is defined as the difference between simulated and barotropic velocity. The downslope area is on the left of the dashed line, and the valley area is on the right. The solid circle indicates the location and time at which KH waves develop, and the dashed circle for TS waves.

Figure 7. The evolution of potential density (σ_θ) for experiment 1 around the sill top at (a) 0.290, (b) 0.295, (c) 0.299, and (d) 0.320 K_1 period, when KH waves develop over the downslope and the shed vortices become smaller over the valley. Each solid and dashed arrow indicates the identical crests of KH waves. The white circle indicates an example of KH billows.

Figure 8. Vorticity (s^{-1}) with potential density contours for experiment 1 over the down slope at 0.320 K_1 period when KH billows develop (corresponding to Fig. 7(d)). The area shown is indicated as region B in Fig. 2. The contour interval is 0.1 σ_θ.

Figure 9. The evolution of the potential density (σ_θ) for experiment 1 around the sill top at (a) 0.338,

(b) 0.365, and (c) 0.405 K_1 period, i.e., during the development and collapse of TS waves in the boundary layer. The area shown is indicated as region A in Fig. 2.

Figure 10. Vertical velocity (cm s^{-1}) with potential density contours for experiment 1 at 0.338 K_1 period (corresponding to Fig. 9(a)) focusing on region D in Fig. 9 (or Fig. 2). The dashed curve shows a phase line of vertical velocity. The contour interval is 0.1 σ_θ.

Figure 11. The potential density (σ_θ) for experiment 3 around the sill top at 0.412 K_1 period. The area shown corresponds to region B in Fig. 2.

Figure 12. Vertical profiles of (a) across-sill velocity and (b) squared buoyancy frequency for experiment 1 at 1.1-km distance and 0.266 K_1 period. Thin and thick lines denote the original and multi-term approximated profiles, respectively.

Figure 13. Results of the stability analysis for the vertical profiles in Fig. 12. The panels on the left are for the case with stratification and those on the right for the case with no stratification. The upper panels denote phase speed (cm s^{-1}) and growth rate (s^{-1}) as a function of wavenumber (m^{-1}), and the lower panels show contours of the stream function of perturbation for a growing mode with a wavenumber of 0.0126.

Figure 14. The spatial distribution of the density variance dissipation rate, χ_ρ, on a logarithmic scale with potential density contours for experiment 1 around the sill top during the first half period at (a) 0.142, (b) 0.181, (c) 0.239, (d) 0.266, (e) 0.290, (f) 0.295, (g) 0.299, (h) 0.320, (i) 0.338, (j) 0.365, and (k) 0.405 K_1 period. Panels (a) to (d), (e) to (h), and (i) to (k) correspond to Figs. 3, 7, and 9, respectively. The contour intervals vary with panels. Shadows within 20 data grids of the sea surface or the bottom indicate areas where χ_ρ is undefined due to the use of the Lanczos filter.

Figure 15. Time evolution of the area-averaged χ_ρ ($<\chi_\rho>$) (thick line) and Φ_d (thin line) for experiment 1 over (a) the downslope (-0.4–2.5 km) and (b) the valley (2.5–4.5 km).

Table 1. Setup of Numerical Simulations [a]

[a] ‘Real topography’ indicates that shown in Fig. 2. In experiment 3, the slope in the lee of the higher ridge is set to be constant and equal to the average in x = 0–2 km in Fig. 2. In experiments 4–12, the turbulence closure model and the Smagorinsky-type model were not used. In all the experiments, P_r is set to be five.

Table 2. Sensitivity Analysis [b]

[b] Here ν_h and ν_z are horizontal and vertical eddy viscosity coefficients (cm^2 s^{-1}), respectively; λ_KH

and λ_{TS} are wavelength of KH and TS waves, respectively; and dash denotes the absence of TS waves.

Table 1. Setup of Numerical Simulations [a]

Experiment	condition at the sill	topography	eddy viscosity coeff.
1	no-slip	real	vary
2	slip	real	vary
3	no-slip	const. slope	vary
4 - 12	no-slip	real	const.

[a] 'Real topography' indicates that shown in Fig. 2. In experiment 3, the slope in the lee of the higher ridge is set to be constant and equal to the average in x = 0–2 km in Fig. 2. In experiments 4–12, the turbulence closure model and the Smagorinsky-type model were not used. In all the experiments, P_r is set to be five.

Table 2. Sensitivity Analysis [b]

Experiment	ν_h	ν_z	λ_{KH}	λ_{TS}
4	500	2	570	-
5	1000	4	620	-
6	2500	10	620	-
7	5000	20	570	-
8	10000	40	550	320
9	25000	100	600	-
10	50	50	500	-
11	500	50	520	550
12	500	500	600	-

[b] Here ν_h and ν_z are horizontal and vertical eddy viscosity coefficients ($cm^2\ s^{-1}$), respectively; λ_{KH} and λ_{TS} are wavelength of KH and TS waves, respectively; and dash denotes the absence of TS waves.

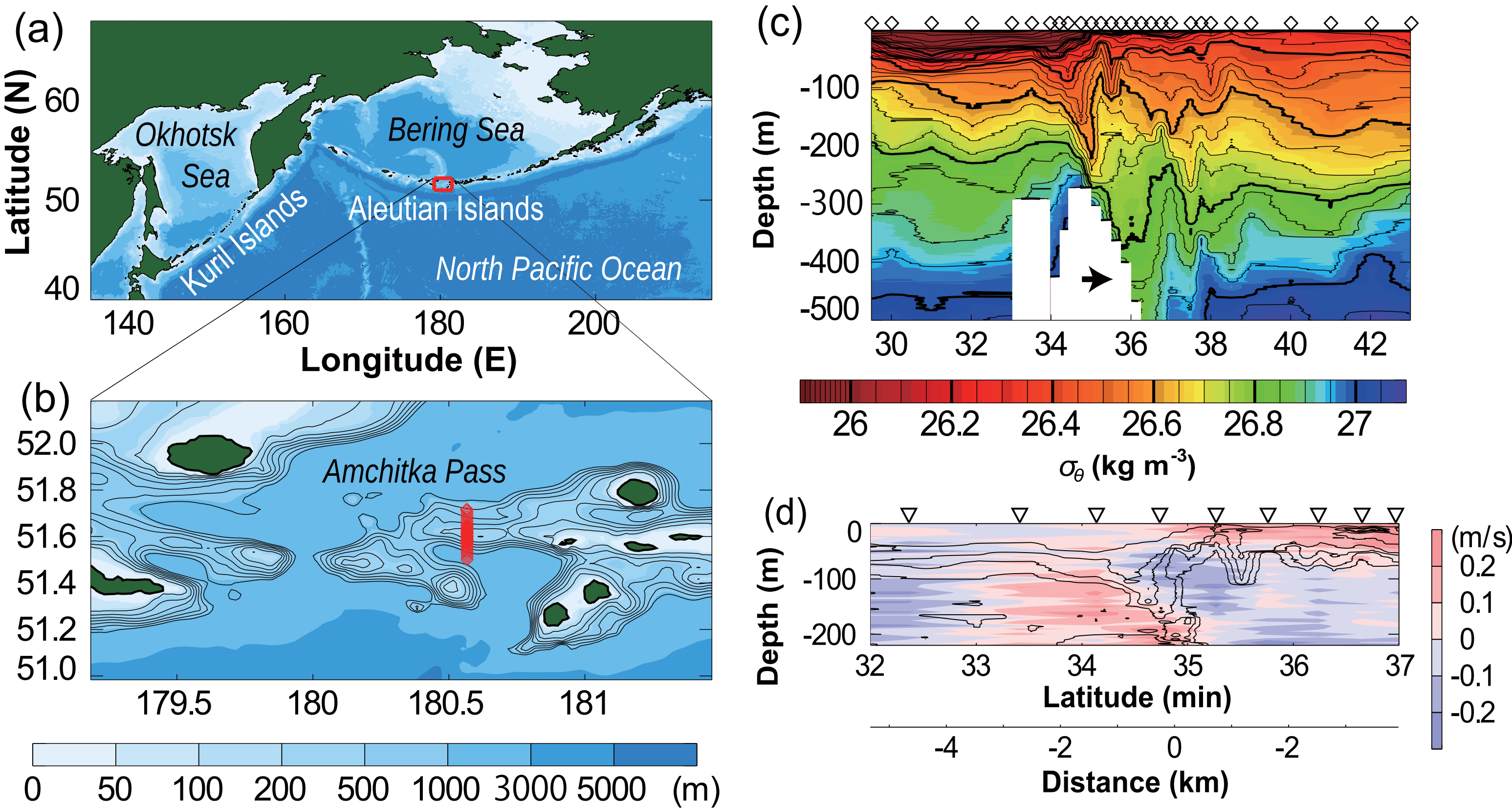

(a)
Okhotsk Sea
Bering Sea
Aleutian Islands
Kuril Islands
North Pacific Ocean
Latitude (N)
60
50
40
140
160
180
200
Longitude (E)
(b)
Amchitka Pass
52.0
51.8
51.6
51.4
51.2
51.0
179.5
180
180.5
181
0
50
100
200
500
1000
3000
5000
(m)
(c)
Depth (m)
-100
-200
-300
-400
-500
30
32
34
36
38
40
42
26
26.2
26.4
26.6
26.8
27
σ_θ (kg m^{-3})
(d)
Depth (m)
0
-100
-200
32
33
34
35
36
37
Latitude (min)
-4
-2
0
-2
Distance (km)
(m/s)
0.2
0.1
0
-0.1
-0.2

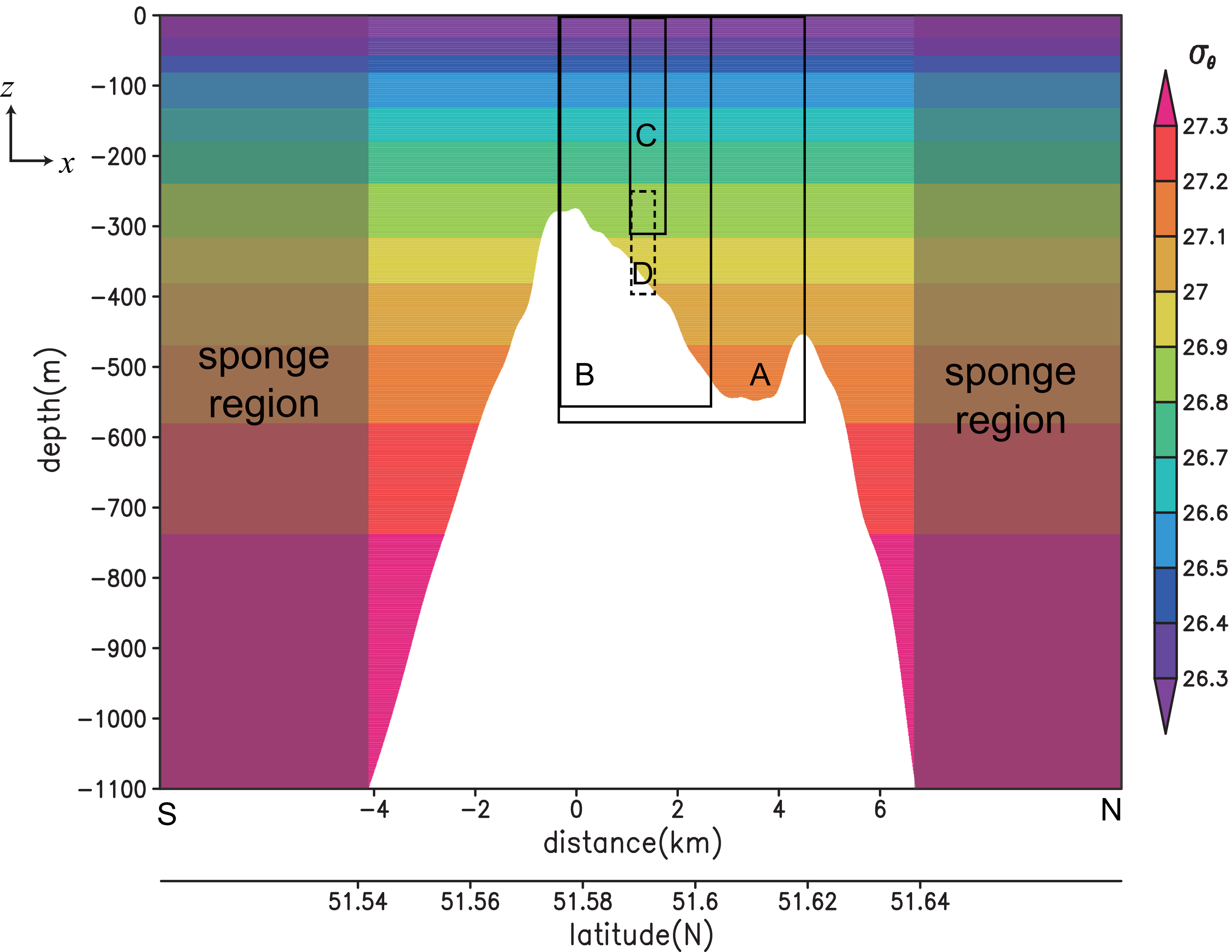

σ_θ
27.3
27.2
27.1
27
26.9
26.8
26.7
26.6
26.5
26.4
26.3
z
x
depth(m)
0
−100
−200
−300
−400
−500
−600
−700
−800
−900
−1000
−1100
sponge region
sponge region
A
B
C
D
S
N
−4
−2
0
2
4
6
distance(km)
51.54
51.56
51.58
51.6
51.62
51.64
latitude(N)

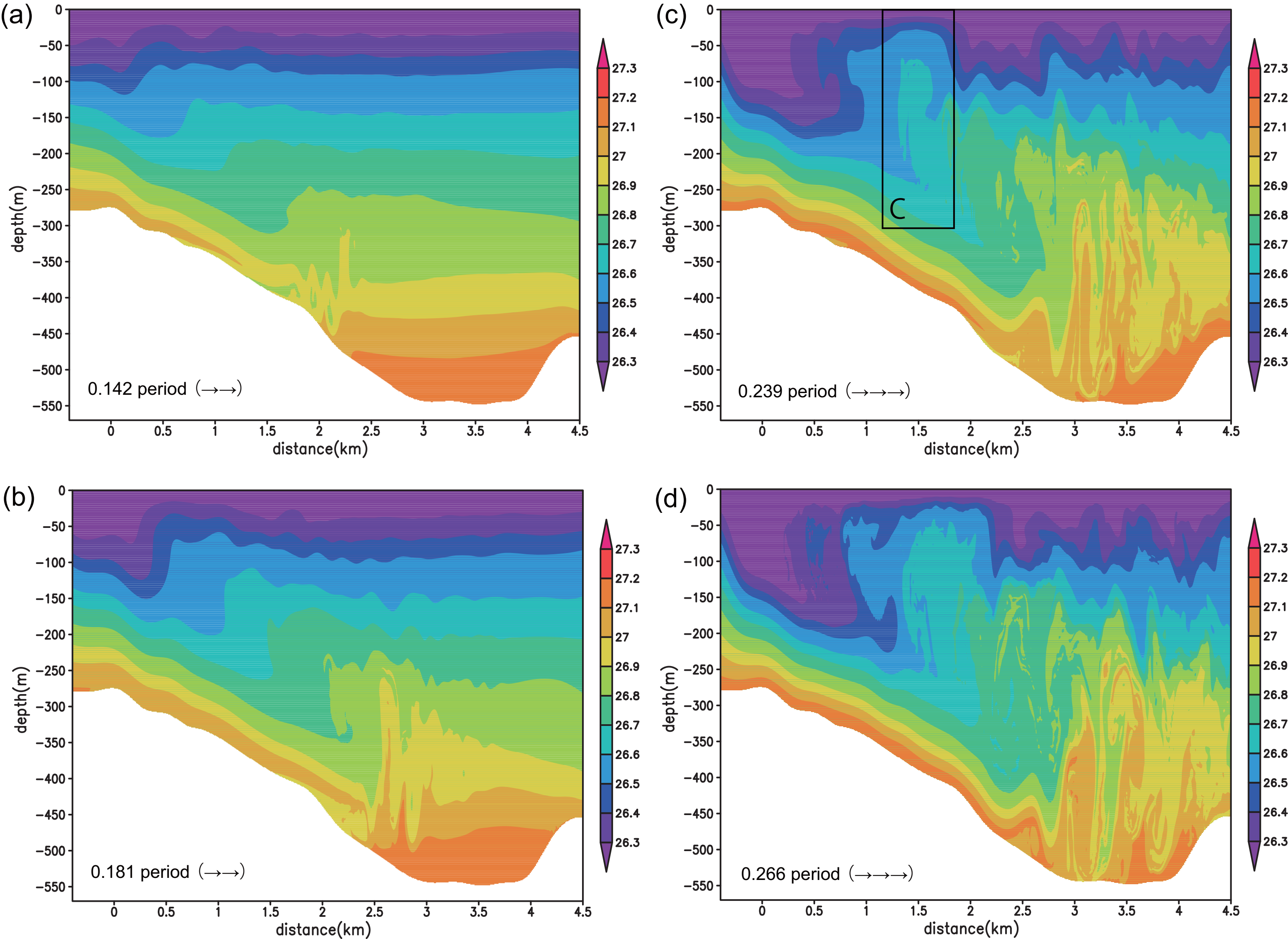

(a)
0.142 period (→→)
(b)
0.181 period (→→)
(c)
C
0.239 period (→→→)
(d)
0.266 period (→→→)
depth(m)
distance(km)
0
-50
-100
-150
-200
-250
-300
-350
-400
-450
-500
-550
0
0.5
1
1.5
2
2.5
3
3.5
4
4.5
27.3
27.2
27.1
27
26.9
26.8
26.7
26.6
26.5
26.4
26.3

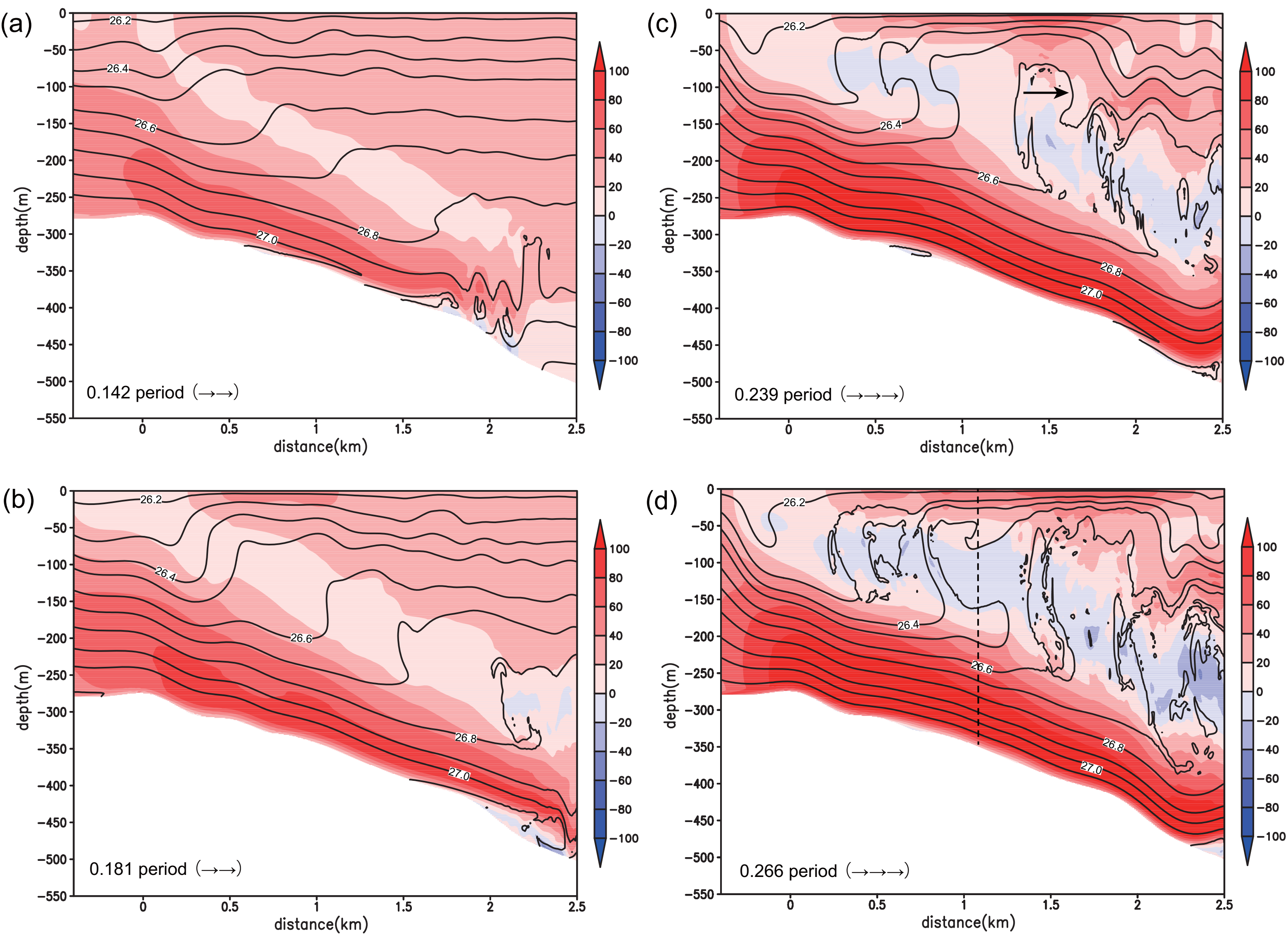
(a)
0.142 period (→→)
(b)
0.181 period (→→)
(c)
0.239 period (→→→)
(d)
0.266 period (→→→)
depth(m)
distance(km)
26.2
26.4
26.6
26.8
27.0
100
80
60
40
20
0
−20
−40
−60
−80
−100

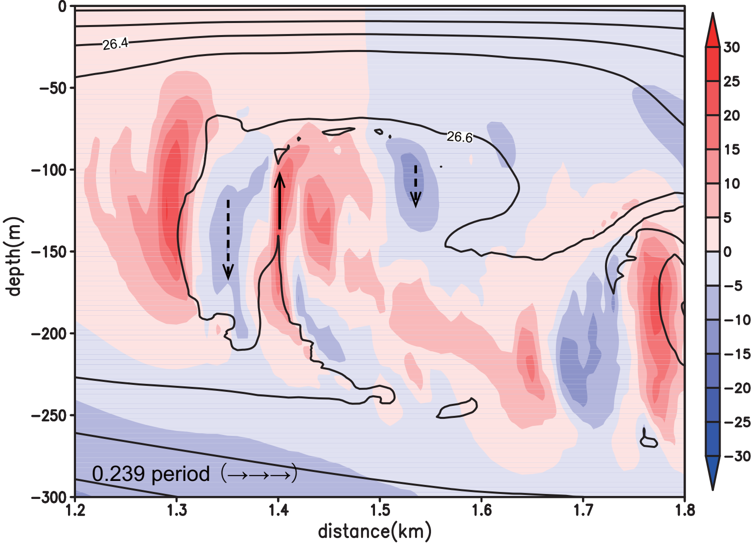

26.4
26.6
0.239 period (→→→)
depth(m)
distance(km)
0
−50
−100
−150
−200
−250
−300
1.2
1.3
1.4
1.5
1.6
1.7
1.8
30
25
20
15
10
5
0
−5
−10
−15
−20
−25
−30

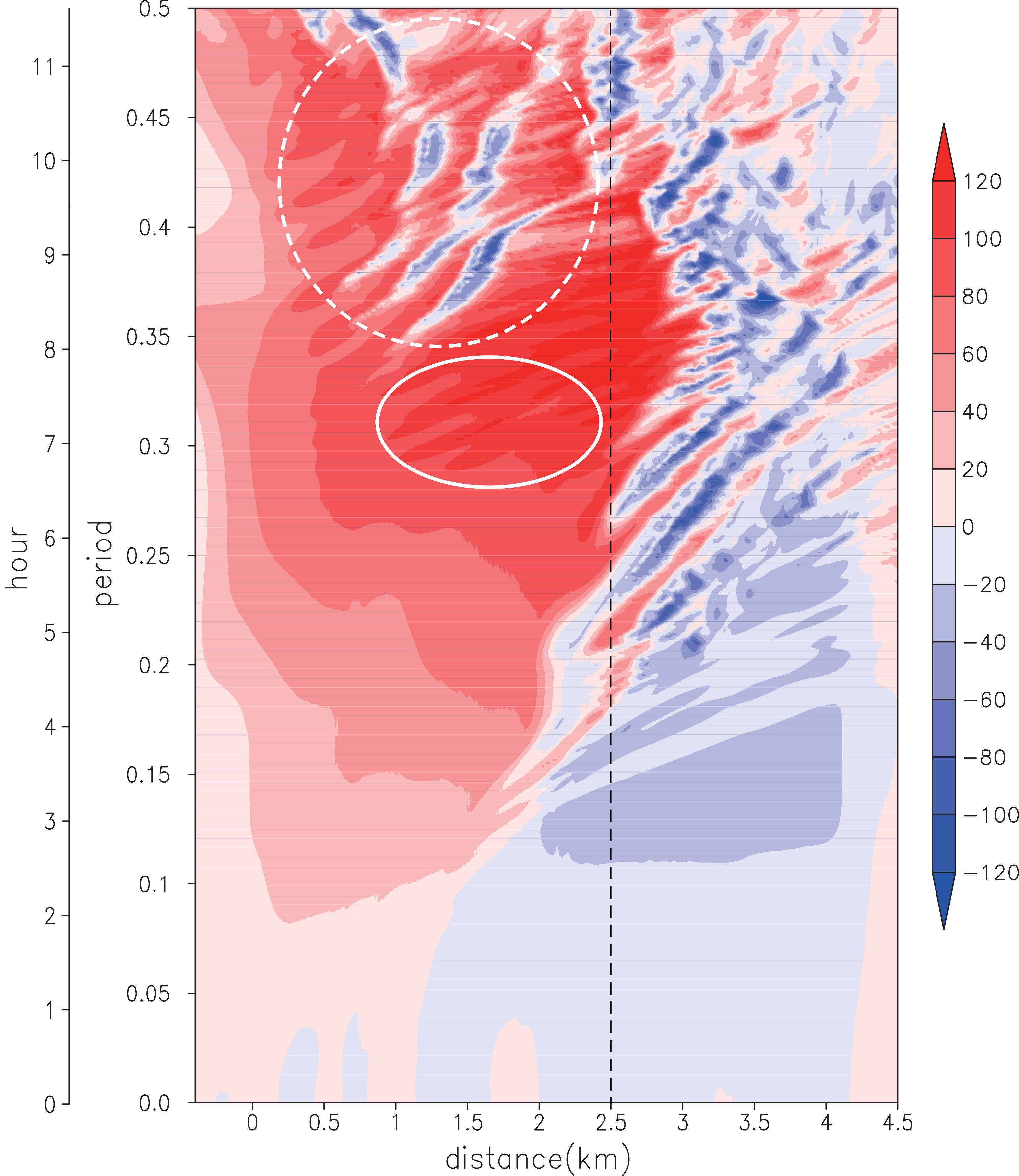

hour
period
distance(km)
0
1
2
3
4
5
6
7
8
9
10
11
0.0
0.05
0.1
0.15
0.2
0.25
0.3
0.35
0.4
0.45
0.5
0
0.5
1
1.5
2
2.5
3
3.5
4
4.5
120
100
80
60
40
20
0
−20
−40
−60
−80
−100
−120

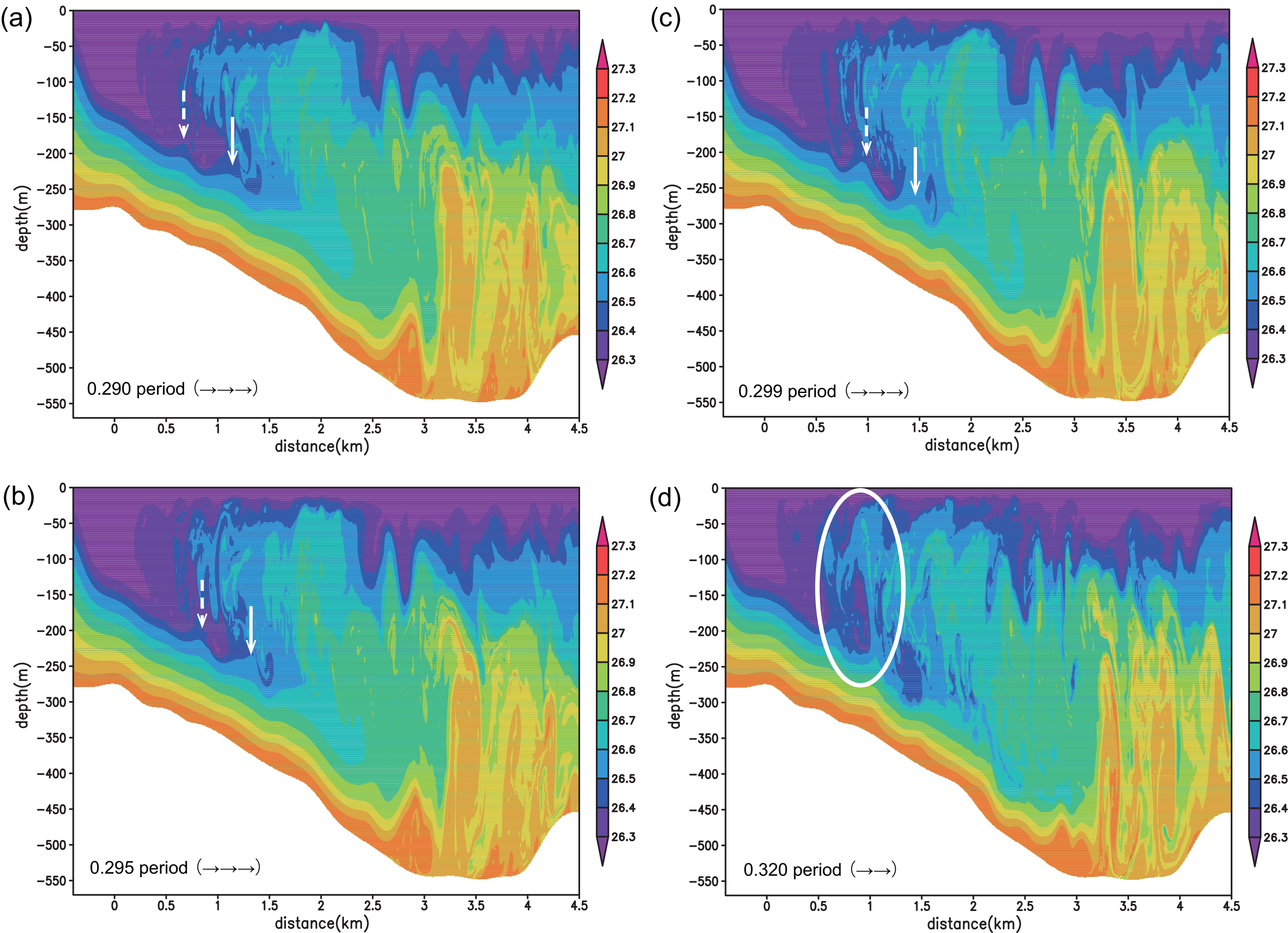
(a)
0.290 period (→→→)
(b)
0.295 period (→→→)
(c)
0.299 period (→→→)
(d)
0.320 period (→→)
depth(m)
distance(km)

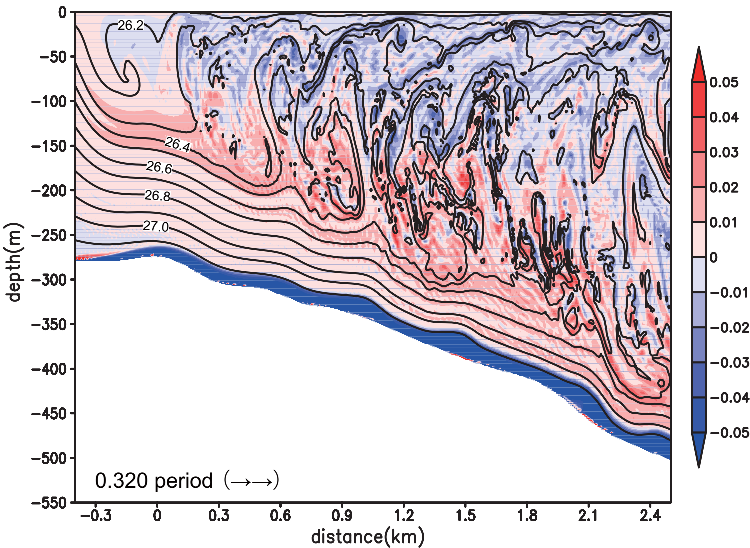

0.320 period (→→)
depth(m)
distance(km)
26.2
26.4
26.6
26.8
27.0
0
−50
−100
−150
−200
−250
−300
−350
−400
−450
−500
−550
−0.3
0
0.3
0.6
0.9
1.2
1.5
1.8
2.1
2.4
0.05
0.04
0.03
0.02
0.01
0
−0.01
−0.02
−0.03
−0.04
−0.05

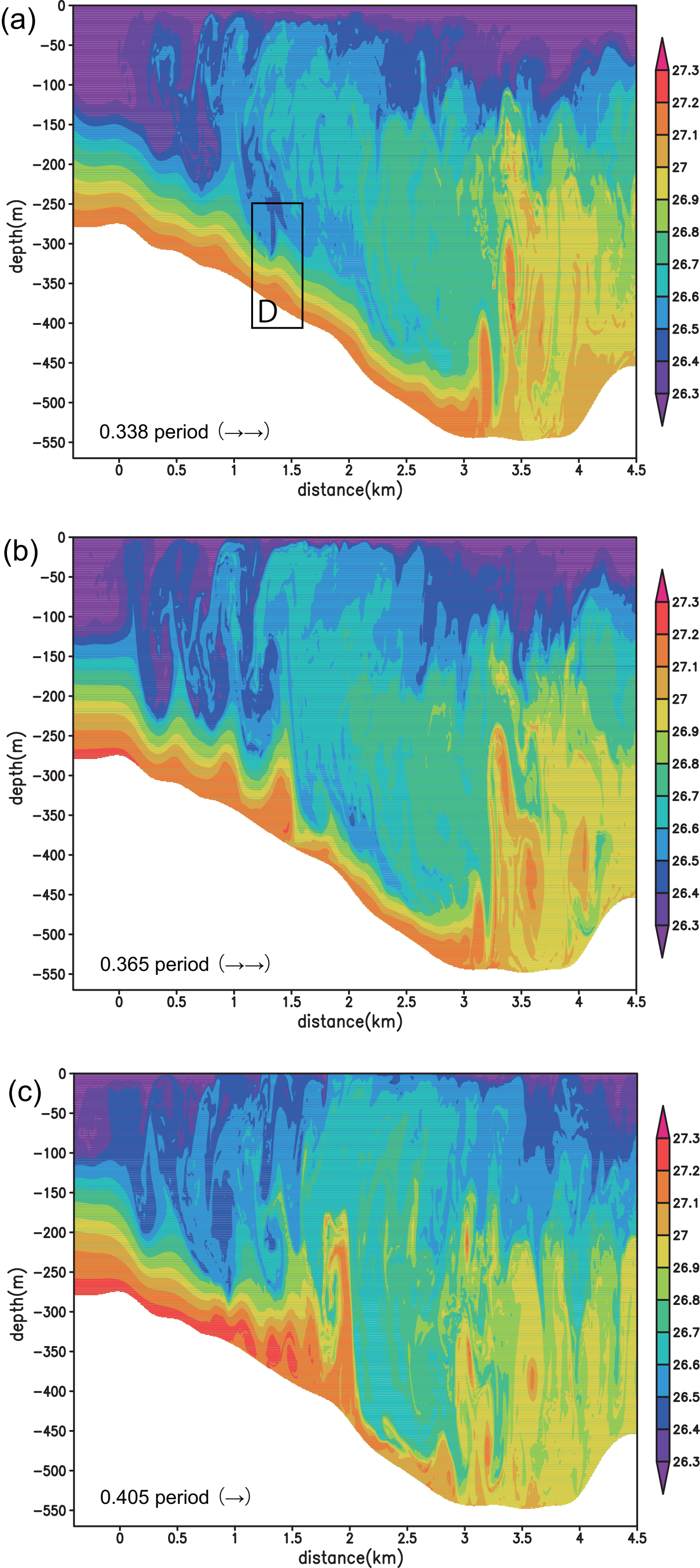

(a)
0.338 period (→→)
D
(b)
0.365 period (→→)
(c)
0.405 period (→)
depth(m)
distance(km)
0
-50
-100
-150
-200
-250
-300
-350
-400
-450
-500
-550
0
0.5
1
1.5
2
2.5
3
3.5
4
4.5
27.3
27.2
27.1
27
26.9
26.8
26.7
26.6
26.5
26.4
26.3

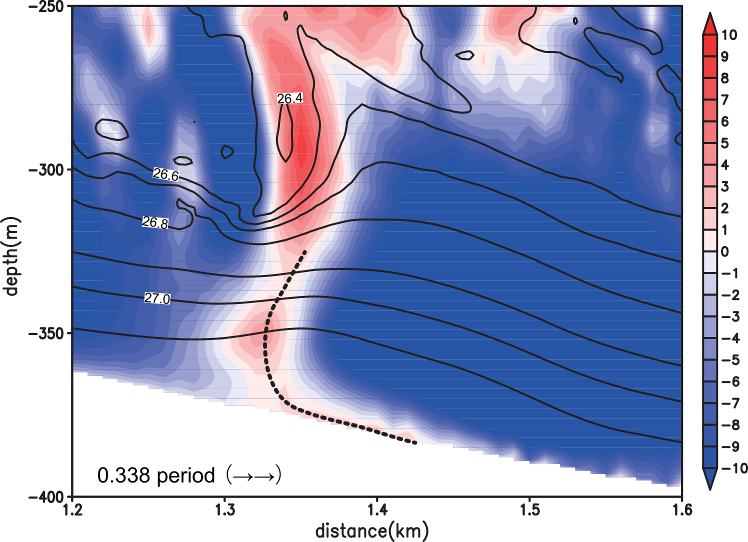

-250
-300
-350
-400
depth(m)
1.2
1.3
1.4
1.5
1.6
distance(km)
26.4
26.6
26.8
27.0
0.338 period (→→)
10
9
8
7
6
5
4
3
2
1
0
−1
−2
−3
−4
−5
−6
−7
−8
−9
−10

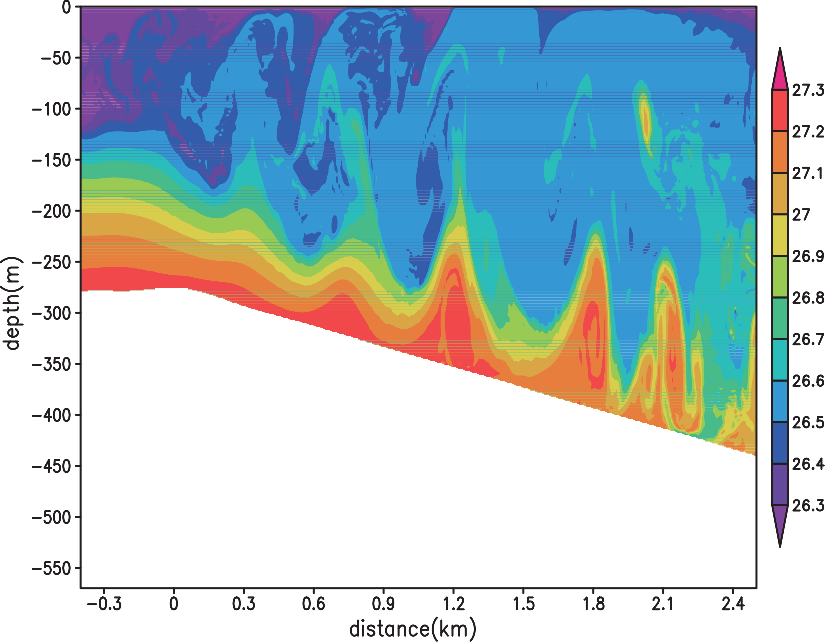

0
−50
−100
−150
−200
−250
−300
−350
−400
−450
−500
−550
depth(m)
−0.3
0
0.3
0.6
0.9
1.2
1.5
1.8
2.1
2.4
distance(km)
27.3
27.2
27.1
27
26.9
26.8
26.7
26.6
26.5
26.4
26.3

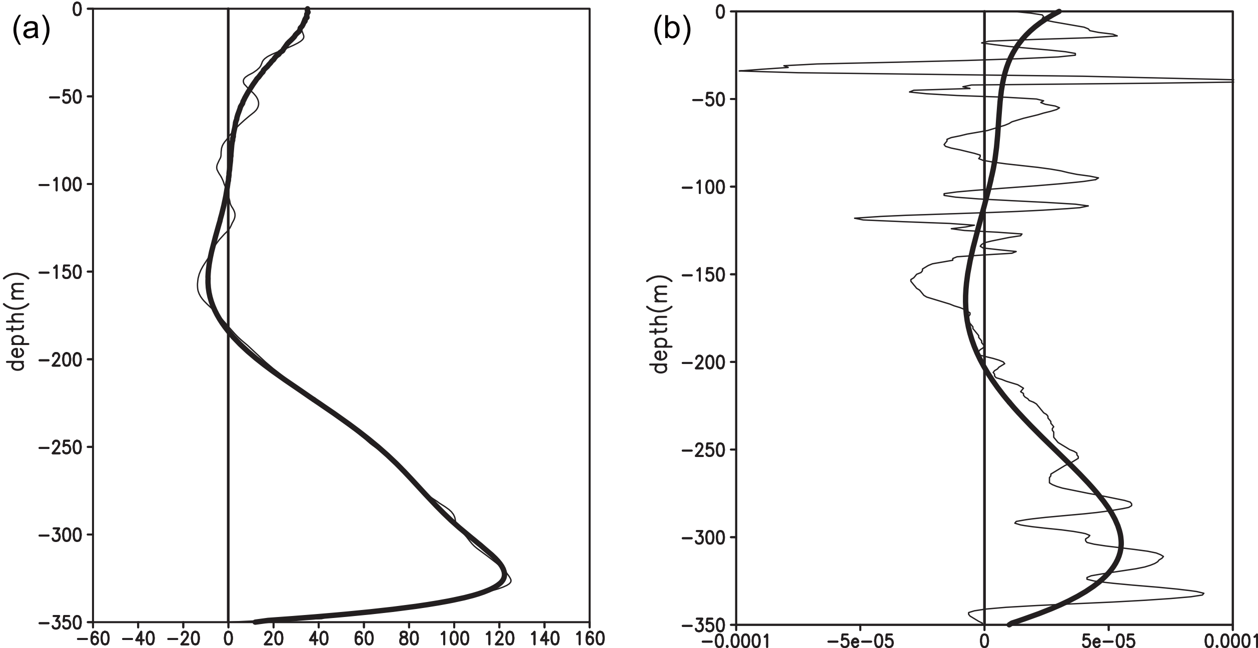

(a)
depth(m)
0
−50
−100
−150
−200
−250
−300
−350
−60 −40 −20 0 20 40 60 80 100 120 140 160
(b)
depth(m)
0
−50
−100
−150
−200
−250
−300
−350
−0.0001
−5e−05
0
5e−05
0.0001

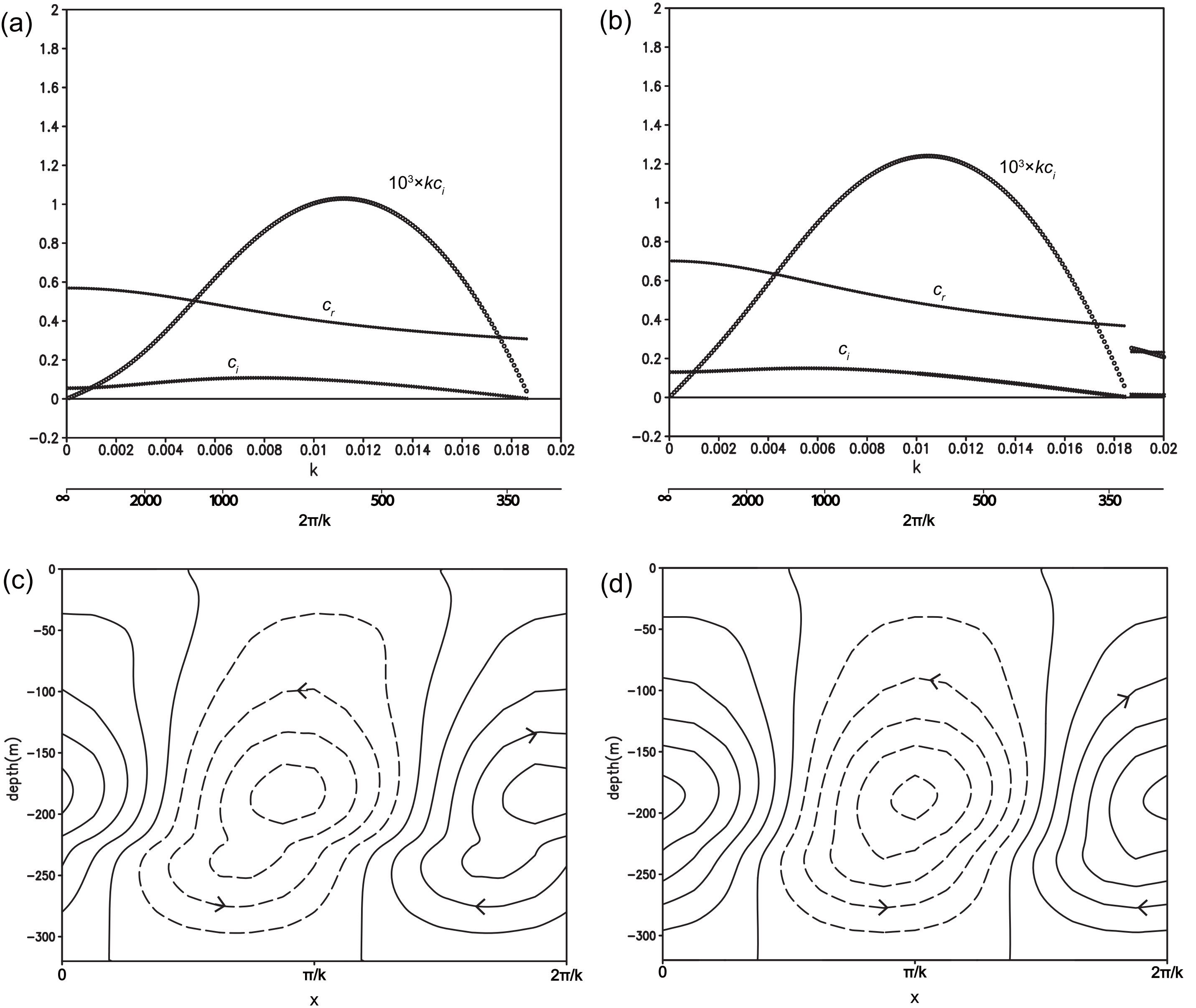
(a)
(b)
(c)
(d)
$10^3 \times kc_i$
c_r
c_i
k
2π/k
∞
2000
1000
500
350
depth(m)
x
0
π/k
2π/k

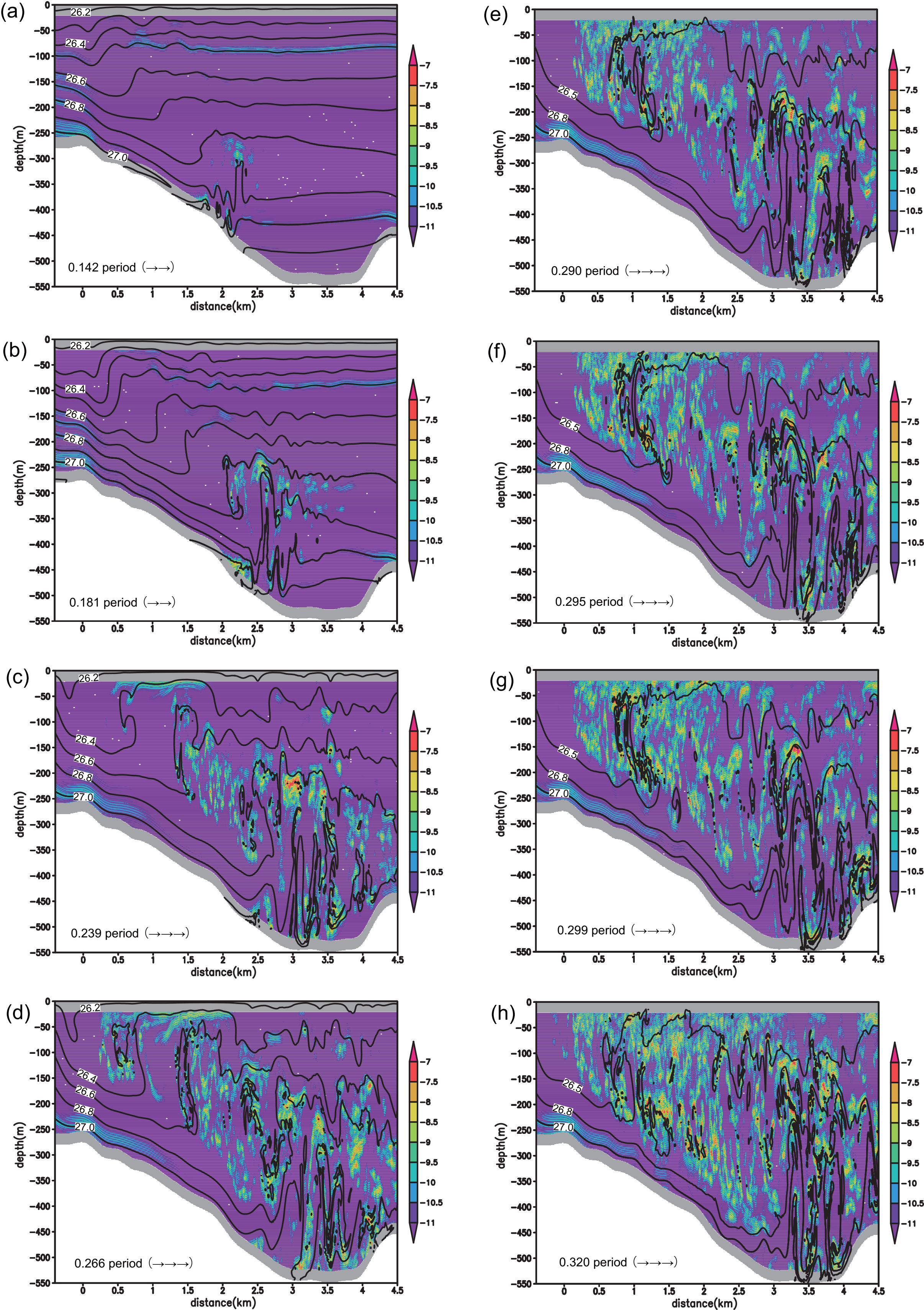
(a)
0.142 period (→→)
(b)
0.181 period (→→)
(c)
0.239 period (→→→)
(d)
0.266 period (→→→)
(e)
0.290 period (→→→)
(f)
0.295 period (→→→)
(g)
0.299 period (→→→)
(h)
0.320 period (→→→)
depth(m)
distance(km)
26.2
26.4
26.5
26.6
26.8
27.0

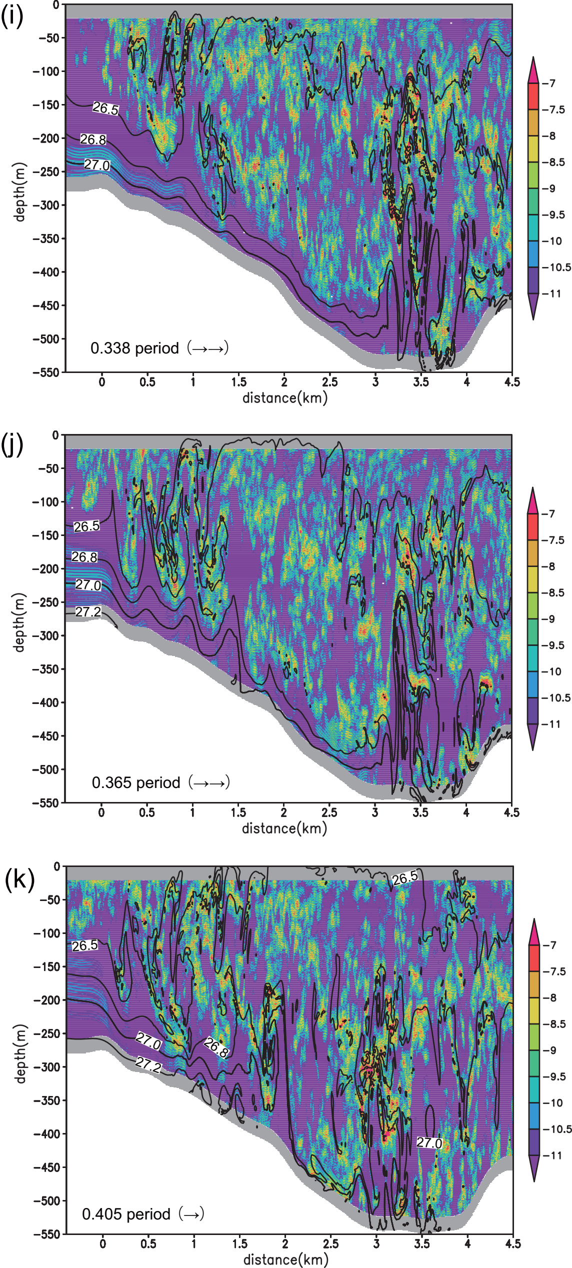
(i)
26.5
26.8
27.0
0.338 period (→→)
depth(m)
distance(km)
0
−50
−100
−150
−200
−250
−300
−350
−400
−450
−500
−550
0
0.5
1
1.5
2
2.5
3
3.5
4
4.5
−7
−7.5
−8
−8.5
−9
−9.5
−10
−10.5
−11
(j)
26.5
26.8
27.0
27.2
0.365 period (→→)
depth(m)
distance(km)
(k)
26.5
26.5
27.0
26.8
27.2
27.0
0.405 period (→)
depth(m)
distance(km)

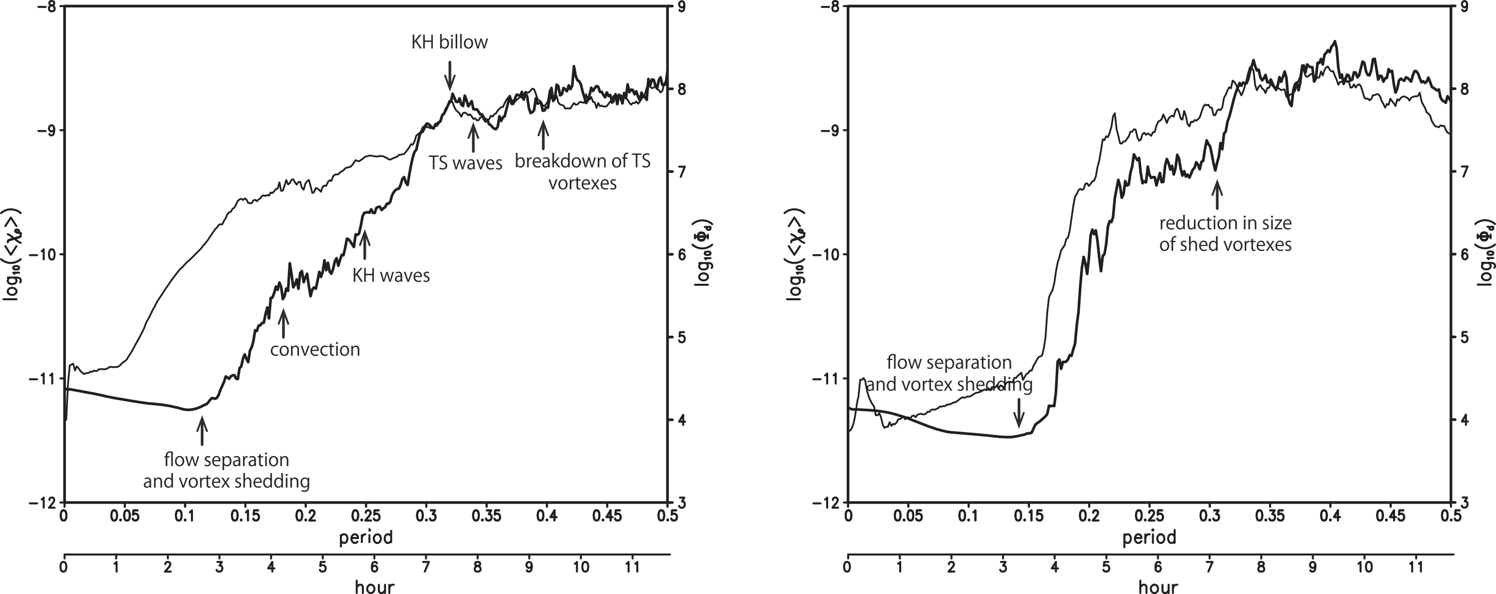

KH billow
TS waves
breakdown of TS vortexes
KH waves
convection
flow separation and vortex shedding
period
hour
$\log_{10}(<\chi_\rho>)$
$\log_{10}(\Phi_d)$
flow separation and vortex shedding
reduction in size of shed vortexes
period
hour
$\log_{10}(<\chi_\rho>)$
$\log_{10}(\Phi_d)$